Energy & Environmental Science

Towards commercialization of colloidal quantum dot solar cells: perspective on device structures and manufacturing

Journal:	*Energy & Environmental Science*
Manuscript ID	EE-REV-10-2019-003348.R1
Article Type:	Review Article
Date Submitted by the Author:	12-Dec-2019
Complete List of Authors:	Lee, Hyunho; University of Illinois at Urbana-Champaign, Materials Science and Engineering Song, Hyung-Jun; Seoul National University of Science and Technology, Safety Engineering Shim, Moonsub; University of Illinois, Materials Science & Engineering Lee, Changhee; Seoul National Univ., School of Electrical and Computer Engineering

Towards commercialization of colloidal quantum dot solar cells: perspective on device structures and manufacturing

Hyunho Lee,†[a] Hyung-Jun Song,†[b] Moonsub Shim*[a] and Changhee Lee*[c]

[a] Department of Materials Science and Engineering, Frederick Seitz Materials Research Laboratory, University of Illinois at Urbana–Champaign, Urbana, IL 61801, USA

[b] Department of Safety Engineering, Seoul National University of Science and Technology, Seoul 01811, Republic of Korea

[c] Department of Electrical and Computer Engineering, Inter-University Semiconductor Research Center, Seoul National University, Seoul, 08826, Republic of Korea

† Hyunho Lee and Hyung-Jun Song contributed equally to this work

*Corresponding authors: mshim@illinois.edu and chlee7@snu.ac.kr

For a past decade, colloidal quantum dot solar cells (CQD-SCs) have been developed rapidly, reaching over 16% power conversion efficiency. Accompanied by the development of materials engineering (CQD surface chemistry) and device physics (structures and defect engineering), CQD-SCs are moving toward commercialization steps. The overview across the board of the requirements for commercialization is timely imperative. Broad comprehensions about structures engineering, upscaling techniques, stability and manufacturing cost of CQD-SCs are necessary and should be established. In this review, development of the device structures is presented with corresponding charge transfer mechanisms. Then, we overviewed the upscaling methods for mass production of CQD-SCs. The comparison between each upscaling techniques suggests the most advanced process closed to the industrialization. In addition, we have investigated the origin of the photovoltaic (PV) performance degradation. The possible degradation sources are categorized by external environmental factors. Moreover, strategies for improving stability of CQD-SCs are presented. Finally, we have reviewed cost-effectiveness of CQD-SCs in terms of niche PV market. The step-wise manufacturing cost analysis for the commercial CQD-SCs are presented. And, the future direction for environmental-friendly CQD-SCs is discussed.

Broader Context

Colloidal quantum dots (CQDs) have received growing attention with respect to solar energy harvesting system on account of possibility of multi exciton generation, easy of energy level control, and solution based process. The efficiency of CQD solar cells have increased rapidly and reached over 16%. It is expected that CQD solar cells will enter a market for non-utility scale, portable, and flexible applications. By utilizing CQD's wide range (~1400 nm) light absorbance characteristics, CQD solar cells can convert low energy infra-red light into electricity, which is barely harvested by conventional crystalline silicon solar cells and or other emerging photovoltaic. Moreover, a stack of low band gap CQD solar cells with conventional (crystalline silicon) photovoltaic system, so called tandem structure, could boost their efficiency by converting low energy IR light into electricity. This review aims to provide comprehensive summary of current status of CQD solar cells in the point of progress of performance and development of device structure. In addition, the key issues of CQD solar cells for realizing large sized stable device are addressed. Moreover, opportunity and challenges for marketability and mass production will be discussed.

1. Introduction

Colloidal quantum dots (CQDs) are chemically synthesized semiconductor nanocrystals whose sizes are typically less than 10 nm. Because of the quantum confinement effect in CQDs, their electrical and optical properties can be easily tuned by modifying their shape and size, which is difficult to achieve in bulk materials. [1] Thus, CQDs have drawn much attention as a highly flexible platform for realizing next-generation optoelectronic devices. Moreover, solution-processed CQDs allow fabrication of devices via a roll-to-roll process, thereby decreasing the manufacturing cost. [2] Consequently, over the last two decades, significant progress has been achieved in the area of CQD-based optoelectronic devices, including light-emitting diodes (LEDs), field-effect transistors (FETs), and photodiodes. [3] Currently, CQD-incorporated LEDs compete with other devices in the high-end display market. [4] Other applications for the development of highly-efficient and commercially-available devices have also been intensively studied.

CQD solar cells (CQD-SCs) are another example having very promising applications. First, these SCs can be fabricated on flexible plastic substrates using a solution-based approach. In addition, CQD films meet the requirements for efficient solar energy harvesting systems in terms of optical and electrical properties. As the absorption coefficients of CQDs are ~ 10^6 cm^{-1}, a film of only a few hundred nanometres is sufficiently thick to absorb sunlight in the range of the CQD bandgap (E_g). [5] Moreover, the E_g of a CQD is easily tuned by varying its size and shape, so the desired E_g can be achieved in the CQD. Thus, a broad spectral range can be harnessed in CQD-based SCs. Furthermore, such cells have the potential to be utilized in tandem devices incorporating other CQDs and/or thin-film SCs. In particular, large-sized CQDs can convert IR light into electricity, which is suitable for the bottom cell of the tandem structure. Regarding the electrical characteristics, the carrier mobility of a well-prepared CQD film exceeds 1 cm^2/Vs, which allows the photogenerated carriers to be transported to the electrode with small losses. [6, 7] Additionally, preferentially oriented carrier transport can be obtained in anisotropic nanostructures, such as nanorods and tetrapods. [8-10] In addition, the energy level of a CQD can be modified by controlling the surface treatment. [11, 12] Different from other bulk semiconductor materials, in CQD films, hot carrier extraction is possible via multiple exciton generation (MEG). Owing to the quantum confinement in a CQD, its efficiency of MEG, in which two excitons are generated from one absorbed high energy photon, is higher than that in bulk semiconductors. [13] Empirically, the external quantum efficiency (EQE) of PbS CQDs has been reported to exceed 100% in the blue and UV regions. [14] Thus, CQD-SCs are expected to be a platform to overcome the Shockley-Queisser limit of a single cell. [15] By exploiting the excellent optical and electrical properties of CQDs, the certified power conversion efficiency (PCE) of CQD-SCs has recently exceeded 16%.

Many materials and compounds have been suggested as solar energy harvesting CQDs. Originally, II-VI CQDs with toxic Cd (CdSe, CdTe and CdS) were adopted in SCs. However, the E_g of these CQDs are large, so their absorption spectrum can only cover the visible light range (up to 800 nm). To utilize a wide solar spectral range extending to the infrared (IR) region, many non-toxic binary (InAs, InP) and ternary ($AgBi_2S$, $CuInS_2$, $CuInSe_2$)-based nanocrystals have been introduced into SCs. [16] Since the bulk films of these compounds exhibit excellent photovoltaic (PV) properties, highly efficient devices were expected to be fabricated when employing these non-toxic CQDs within the devices. However, the device efficiency of these CQD-SCs is not very high because of the poor understanding of their energy level, poor size control, and lack of a good synthesis method. To date, most record high results have been obtained from SCs with PbS and PbSe nanocrystals, which absorb a broad range of solar

spectrum from UV to IR.

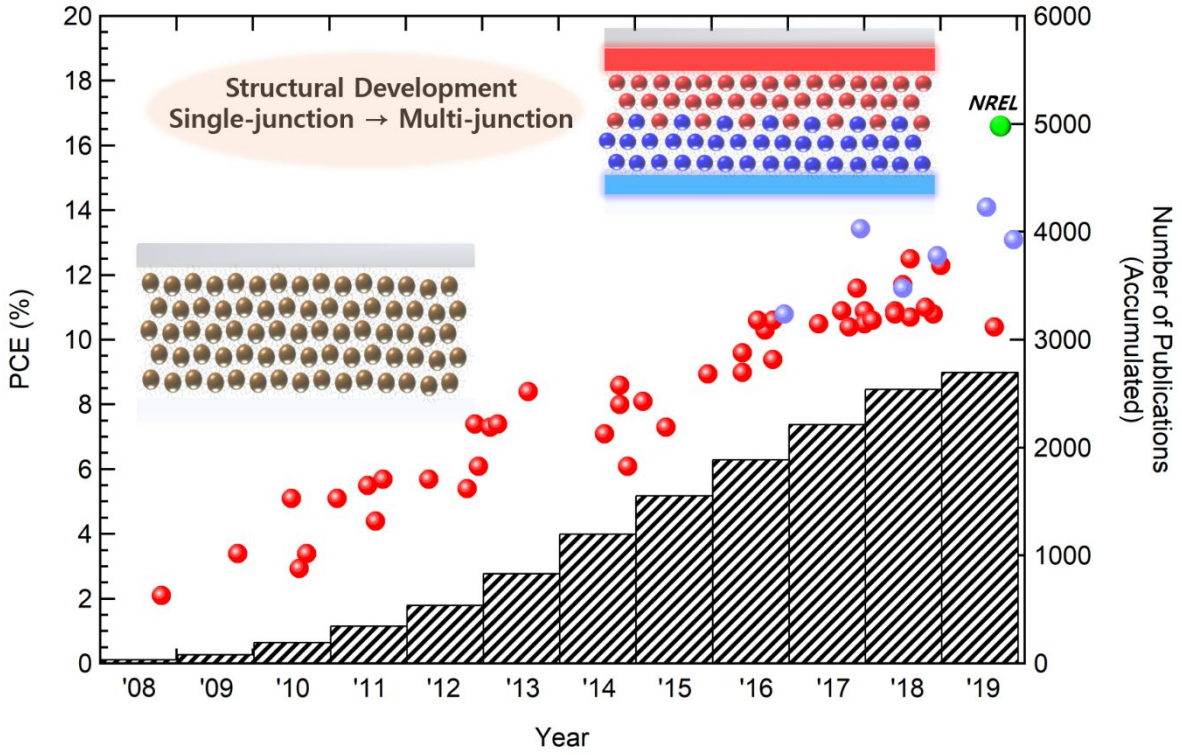

Fig. 1 PCE development of CQD-SCs based on the accumulated number of publications over years. Each plot of the PCE is based on the table 1. Red dots represent PbS and PbSe based CQD-SCs. Sky-blue dots represent $CsPbI_3$ CQD-SCs. Green dot represents PCE record by NREL. The type of active layer has not been reported. (Web of Science, search by quantum dot solar cells; colloidal quantum dot solar cells)

Fig. 1 shows the development of the PCE of CQD-SCs (Pb based) and the number of publications over time. Over two thousand studies have been reported since 2008, contributing to the improvement of the PCE over the past decade. The field of CQD-SCs is now moving towards their commercialization with featured advantages of CQDs. Although intensive studies have been conducted to improve efficiency and stability of CQD-SCs, it is still lab-scale and proto-type devices compared to other type solar cells. According to the market survey from the Fraunhofer Institute of Solae Energy (ISE, Germany) and National Renewable energy laboratory (NREL, United States), the annual installation of photovoltaic system exceeded 90 GW in 2018. Among many types, crystalline silicon (C-Si) and other thin film based cells (CdTe, Cu-In-Ga-Se, armorphous Si and GaAs) are competing in the PV market, and their manufacturing facilities are already over GW scale (Please see Fig 2.) [17, 18] On the other hand, other emerging technologies, including CQD, perovskite, organic and so on, are still on the stage of developing performance of proto-type devices. In current status, only few companies (e.g. QD solar , Quantum materials corp.) aim to demonstrate commercially available CQD SCs, while others (e. g. Nanosys, Nanoco, QD vision and so on) focus on improving the electrical and optical properties of QD itself. Nevertheless, as performance of CQD-SCs has enhanced significantly in last decade, it is expected that they will enter the flexible solar cell market very soon. To occupy the proper PV market share, several issues should be handled, such as the efficiency, mass-production device structures, manufacturing process, device

stability and cost effectiveness of the materials as well as fabrication. Although progress and research trend of CQD SCs have been clearly summarized in other review papers, the approach for commercialization of CQD-SCs has been barely addressed. Considering the progress in CQD-SCs, it would be fruitful to figure out current status of CQD SC technologies and their possible commercialization for further future studies. In this review, we cover the progress in CQD-SCs towards commercialization. First, the device physics will be discussed in determining the most efficient device structures and device engineering methods to date. Then, we will discuss the viability of upscaling the manufacturing process of CQD-SCs for mass production. Furthermore, progress in the stability of the devices will be reviewed along with degradation mechanisms involving internal or external degradation sources. Finally, the possible approaches towards commercialization of CQD-SCs will be reviewed considering cost and environmental issues.

Table 1. PCE development of CQD-SCs.

Published Year	PCE (%)	Reference (Type of Active Layer)
2008	2.1	PbSe [19]
2009	3.4	PbSe [20]
2010	2.9~5.1	PbS [21-23]
2011	5.1~5.7	PbS [24-27]
2012	5.4~7.4	PbS [28-31]
2013	7.3~8.4	PbS [32-34]
2014	6.1~8.6	PbS [35-38]
2015	7.3~9.0	PbS [39-41]
2016	9.0~10.6	PbS [12, 42-46], $CsPbI_3$ [47]
2017	10.4~11.6	PbS [48-53], $CsPbI_3$ [54]
2018	10.6~12.5	PbS [2, 55-62], $CsPbI_3$ [63, 64]
2019	10.4~16.6	PbS [65], $CsPbI_3$ [66, 67], Etc.[18]

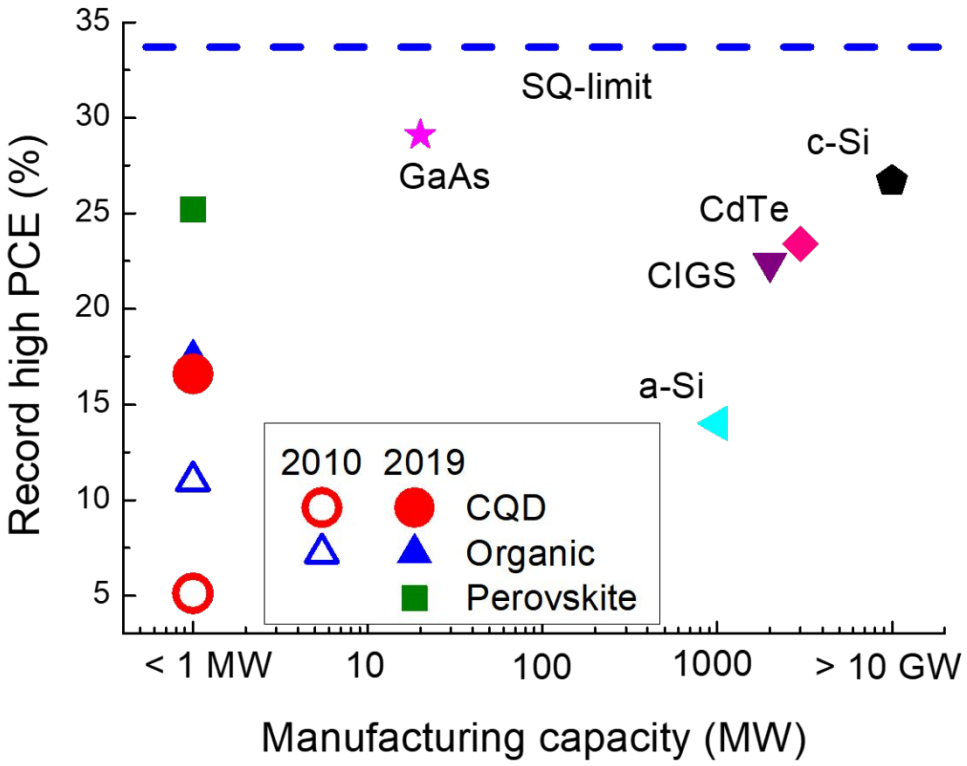

Fig. 2 Record high efficiency and manufacturing capacity of various type of photovoltaic cells. Five technologies, based on c-Si, CdTe, Cu-In-Ga-Se (CIGS), amorphous silicon (a-Si), and GaAs, compete each other in the market, while other emerging solar cells are still proto type devices. However, the efficiency of emerging solar cells have increased rapidly for ten years, it would be expected that they will enter the market commercialized in near future.

2. Device physics

2.1 Device structures

The device structure is the most important factor that affects charge generation and transport in CQD-SCs. Device structures have been developed to extend the depletion region in the CQD layer and optimize energy level alignment for efficient charge extraction to electrodes. This section addresses the development of the device structures in terms of charge generation, transport mechanisms, and ultimately PV performance.

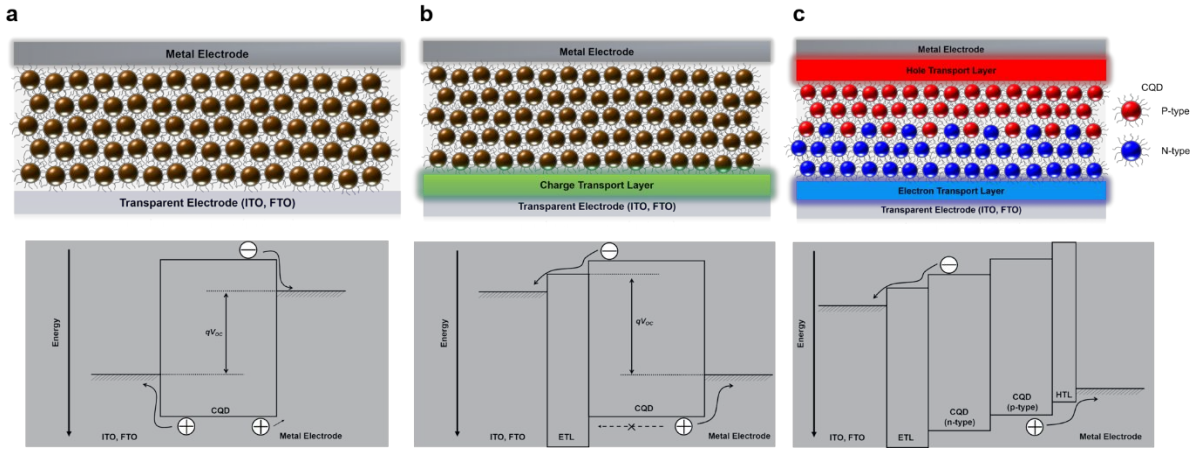

Fig. 3 Schematic diagram of device structures and the energy level bands. (a) Schottky CQD-SCs. (b) Depleted heterojunction CQD-SCs. (c) Quantum junction or band alignment CQD-SCs.

2.1.1 Schottky CQD-SCs

Schottky CQD-SCs were the first proposed device structure, in which the CQD active layer is sandwiched between a transparent electrode (ITO (indium tin oxide) or FTO (fluorine-doped tin oxide)) and a counter metal electrode. N-type or p-type CQD films form Schottky junctions with counter metal electrodes (Fig. 3(a)). A potential difference at the junction leads to charge extraction of photogenerated carriers from the CQD layer to each electrode. In theory, the height of the Schottky barrier is estimated by the difference in the work functions of each electrode (Fig. 4(a)). However, experimental results showed that the barrier heights are normally less than the difference in the work functions of each electrode. [68] The E_g of a CQD changes depending on the size of the nanocrystals. The E_g energy increases as the nanocrystal diameter decreases. The shorter first excitation wavelength of smaller CQDs results in an open circuit voltage (V_{OC}) improvement. The work function difference between metal electrodes (Ca, Mg, Ag, Al and Au) results in different V_{OC} as well as different Schottky barriers as shown in Fig. 4(b). [19] Thickness control of a ligand-exchanged CQD layer enabled improvement of the PV performance, achieving a 5.2% PCE. [69] In addition, CQD layers were oxidized to enlarge the Schottky barrier height by air annealing and UV-ozone treatment. An oxidized PbS film induces a hole injection barrier that leads to a built-in voltage improvement. [70] Moreover, insertion of a buffer layer between the electrodes and CQD layer provides an increased energy barrier, thereby resulting in better carrier transport. A thin LiF layer was applied to enhance the Schottky barrier stability at the interface between the CQD layer and metal electrode. [71] The work function of FTO was tuned by inserting polyelectrolyte (polyethylenimine, PEI), increasing the Schottky junction barrier at the CQD/FTO interface. [72] Nevertheless, the limitation on the Schottky barrier height tuning and the weak stability of the Schottky junction of CQDs mitigate the advantages of easy fabrication process and simple device structure of Schottky CQD-SCs. To date, the reported V_{OC} of Schottky CQD-SCs is far below the expected V_{OC} based on the CQDs' E_g. Nevertheless, Schottky CQD-SC structures are efficient tools for investigating CQDs' material characteristics, such as carrier mobility, diffusion lengths, and doping concentrations of CQD films.[12]

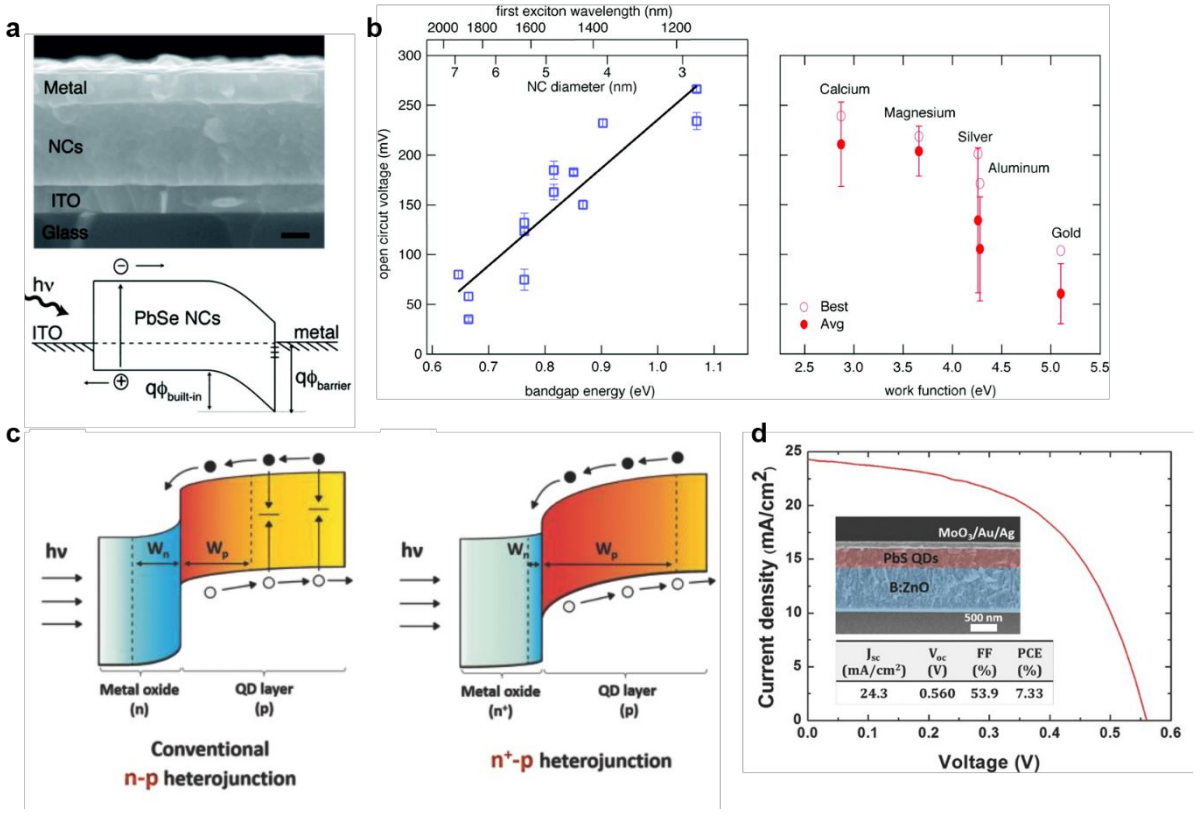

Fig. 4 Schottky and depleted heterojunction CQD-SCs. (a) Cross sectional scanning electron microscopy (SEM) and schematic diagram of Schottky CQD-SC. Scale bar represents 100 nm. (b) V_{OC} trends of Schottky CQD-SCs with different CQD sizes (different E_g) and work function of metal electrode. Reproduced permission from ref. [19]. Copyright 2008, American Chemical Society. (c) Schematic energy band diagram of conventional and n-doped ETL employed depleted heterojunction CQD-SCs. (d) *J-V* characteristic of depleted heterojunction CQD-SC with boron doped ZnO layer as a transparent electrode. The inset represents cross sectional SEM image of the device and the photovoltaic performance table. Reproduced permission from ref. [73]. Copyright 2016, Wiley.

2.1.2 Depleted heterojunction CQD-SCs

Depleted heterojunction CQD-SCs are motivated by p-i-n-based PV devices. CQD layers are deposited on top of wide E_g oxides (TiO_2 or ZnO), forming junctions with the electron transport layers (ETLs). The introduction of a junction between the ETL and CQD allows one of the main limitations of Schottky CQD-SCs to be overcome (Fig. 3 (b)). Photogenerated charge carriers are created in the junction region and can be efficiently extracted by the ETLs. Furthermore, the ETLs block hole transport from the CQD layers to the cathode, thereby resulting in reduced non-radiative electron-hole recombination. Early studies on depleted heterojunctions focused on energy level alignment between the CQD layers and charge transport layers (CTLs) by controlling the CQD diameter or thickness. [20, 74] A comparison between depleted heterojunction and Schottky-type SCs revealed that higher V_{OC} and *FF* can be obtained by implementing proper CTLs. [75] E_g tuning of CQDs allows the formation of different junction kinetics at the interfaces, resulting in a 5.1% PCE. [23] Most studies focused on modification of ETLs. ZnO nanoparticles were used as ETLs and formed heterojunctions with 1.3 eV bandgap PbS QDs, resulting in a certified 2.94% PCE with 1000-hour stable cells.

[21] Mesoporous TiO_2 also elongated the depletion region between the ETL and the CQD layer, which improved charge extraction at the junction region. Thus, thicker CQD layers could be applied, which resulted in enhanced light absorption. As a result, the short circuit current density (J_{SC}) increased by almost two-fold, and a 5.5% PCE was achieved. [24] For better charge collection efficiency, mesoporous TiO_2 was modified to a more periodic pillar structure. The charge carriers generated at the deeper region in the device were optically demonstrated to be efficiently extracted by the periodic ETLs. This modification extended the depletion region twofold and led to a hysteresis-free 5.7% PCE. [29] Mesoporous type CQD-SCs were further optimized with a TiO_2 nanonetwork structure, and a 7.3% PCE was achieved. [32] In addition, UV-ozone treatment of ZnO allowed control of the depletion region area. The corresponding thickness of the CQD layer could be increased, which resulted in an enhanced PCE. [76] ZnO was also modified to nanowire structures to enlarge the surface area of the thick depletion region. The use of highly n-doped ZnO layers with boron doping increased the depletion region at the junction side (Fig. 4(c)). A 7.55% PCE was reported for CQD-SCs employing n-doped ZnO, and even when the n-doped ZnO layer was used as a transparent electrode, a 7.33% PCE was obtained (Fig. 4(d)). [73] Chemical modification of the ZnO surface reduced its surface trap sites. Photogenerated charge carriers in the depletion region were efficiently extracted by a 1,2-ethanedithiol (EDT) ligand-treated ZnO layer, resulting in a 10.14% certified PCE. [43] Additionally, metal oxide and p-type polymer layers are widely adopted as a hole transporting layer (HTL) in CQD-SCs. The optimization of CQD layers by introducing a MoO_3 layer at the hole contact electrode resulted in a 4.3% PCE. [77] Recently, PBDTTT-E-T, a copolymer of benzo[1,2-b:4,5-b′]dithiophene (BDT) and thieno[3,4-b]thiophene (TT), was introduced as an HTL in IR CQD-SCs. [78] In addition, the introduction of a nanostructure HTL into the device, using nanoimprint lithography, enhanced light absorption at the IR wavelengths. As a result, a record PCE (19.1 mW/cm^2, cutoff < 1100 nm) of 6.83% was obtained under IR light (19.1 mW/cm^2, cutoff < 1100 nm), which is suitable for tandem structures with commercialized c-Si SCs (absorbing light up to 1100 nm).

2.1.3 Quantum junction CQD-SCs

A heterojunction between inorganic CQDs was introduced to CQD-SCs in 2012 by Rath et al. [79] The purpose of a quantum junction is to extend the depletion region at the junction area. The photogenerated charge carriers can be efficiently separated at the junction region in the active layer. n-type Bi_2S_3 CQDs and p-type PbS CQDs were used as a heterojunction. The advantage of the heterojunction layer was an improved carrier lifetime, which minimizes recombination losses. Thickness and mixing ratio optimization of the QD junction resulted in a 4.87% PCE. The E_g of PbS CQDs was controlled (0.6 ~ 1.6 eV) to align the energy levels of different quantum junctions. E_g matching between n- and p-type CQDs resulted in a 5.4% certified PCE. [31] Furthermore, a comparison of the simulated efficiency trends between depleted heterojunction and quantum junction CQD-SCs demonstrated that the quantum junction has high potential for a higher PCE by managing the E_g of the quantum junctions. The initial stage of quantum junction SC research used Schottky-type cell structures. The order of the quantum junction (np- or pn-wise stacking) and corresponding metal electrode could be controlled to activate SCs under a forward or reverse bias current. [80] Quantum junction cells were further improved by applying additional charge extraction layers. TiO_2- and aluminium-doped ZnO (AZO) ETLs were introduced into PbS quantum junctions. A 6.1% PCE was achieved by adding MoO_3 at the hole contact. [37] Furthermore, halide exchange has been intensively studied to utilize different doped CQDs as shown in Fig. 5(a). Highly n-doped iodide-modified PbS

CQDs, n-doped bromide-modified PbS CQDs, and p-doped mercaptopropionic acid (MPA)-modified PbS CQDs were applied to form a ternary junction, which extended the depletion region to approximately 330 nm (Fig. 5(b)). As a result, an 8.0% PCE was reported. [38] The size of CdSe CQDs were tuned to realize proper band alignment between a ZnO ETL and PbS CQDs. The photogenerated charge carriers from the PbS CQDs as well as from the CdSe CQDs contributed to an improved J_{SC}, thereby leading to a 7.5% PCE. [81] n- and p-type CQDs were synthesized by the pre-ligand exchange method. The np quantum junction arising from pre-synthesized CQDs on top of a ZnO ETL showed a 10.94% PCE without a complicated washing process. [55]

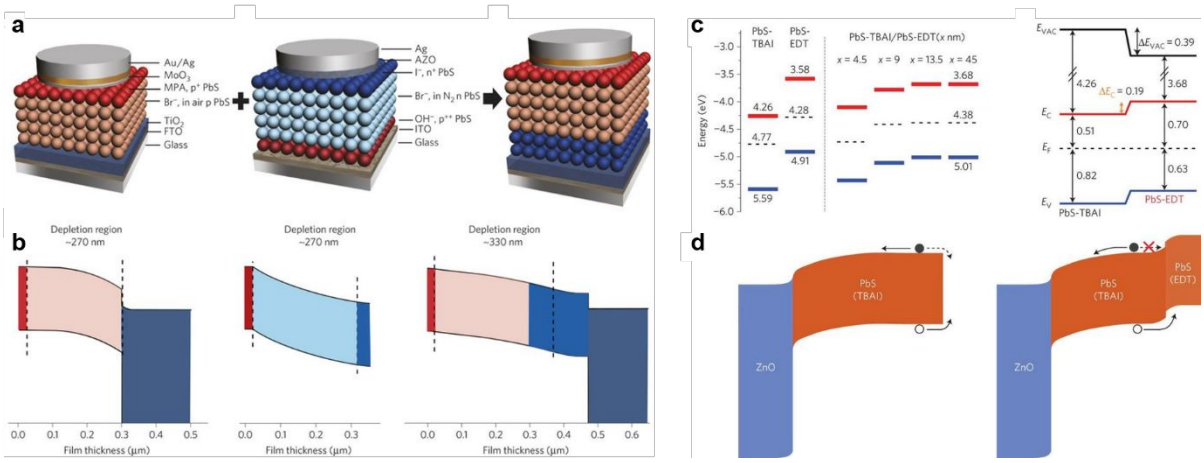

Fig. 5 Quantum junction and band alignment CQD-SCs. (a) Schematic of ternary quantum junction by combining conventional (p-p^+ junction) and inverted (p^{++}-n-n^+) quantum junction structures. (b) Corresponding simulated energy band diagram with depletion regions. Reproduced permission from ref. [38]. Copyright 2014, Springer Nature. (c) Energy levels of pure PbS-TBAI, PbS-EDT and PbS-TBAI with different thicknesses of PbS-EDT layers. Red and blue lines represent conduction and valance band edges of CQDs. Dashed lines represent fermi levels of each CQDs. (d) Proposed energy band bending at short-circuit conditions. Reproduced permission from ref. [35]. Copyright 2014, Springer Nature.

2.1.4 Band alignment

The structural development of CQD-SCs has been moving towards enlarging the depletion region and reducing the energy barrier at the junction between CQDs and CTLs for efficient charge extraction as shown in Fig. 3(c). The band alignment structure of CQD-SCs aims to enhance these parameters by introducing additional CTLs and ligand exchange of CQDs. For p-doped CQDs, the surface of CQDs was treated with a short cross-linking ligand, 3-mercaptopropionic acid (MPA) or 3-mercaptobutyric acid (3-MBA). The p-doped CQDs with 3-MBA exhibited a larger depletion region, and the p+-doped CQDs with MPA exhibited a larger quasi-Fermi level splitting, leading to a higher V_{OC}. The combination of both ligands resulted in gradient band alignment with a 7.2% PCE. [82] Tetrabutylammonium iodide (TBAI) and EDT were applied to CQDs as n- and p-type ligands, respectively. EDT-PbS CQDs showed band alignment with TBAI-PbS CQDs and even took on the role of electron blocking in the hole contact region (Fig. 5(c) and (d)). An 8.55% certified PCE was recorded. [35] To estimate the underlying mechanism of carrier transport in TBAI- and EDT-capped CQDs, temperature-dependent electrical characterization of CQDs were conducted. Based on carrier lifetime, electron and hole diffusion length, doping concentration, and depletion width measurements, a

highly p-doped CQD was required for V_{OC} improvement. Moreover, the concentration of the p-type dopant should be one order of magnitude higher than that of the n-type dopant for efficient band alignment. [12] Ligands were further exchanged with methylammonium lead iodide ($MAPbI_3$) and thioglycerol (TG). Both $MAPbI_3$ and TG ligand exchange led to n-type properties. When n-type CQDs were mixed together, the charge transfer between the valence bands (VBs) of the mixed n-type CQDs was efficient compared to that in single CQD films. Thus, in the donor-acceptor structure CQDs, the appropriate donor-acceptor ratio leads to balanced electron-hole pairs. As a result, a hysteresis-free 10.45% PCE was reported. [52] Moreover, E_g control of IR-absorbable CQD ink, dissolved in a highly stable non-polar solvent, led to the formation of a graded back junction and an extended depletion region. A mixture of 1.4 eV and 1.3 eV n-type CQDs further absorbed light in the IR region, resulting in a 12.3% PCE. [59] However, the introduction of the junction between HTL and CQDs has been less studied compared to ETL junctions because realizing smooth band alignment at the interface was difficult, and serious recombination frequently occurred at the interface. Furthermore, CTLs beneath of CQD layers need to be robust to endure chemical processes such as ligand exchange and CQD surface treatments. The high level of requirements for CTLs limited the materials. Wang et al. inserted a NiO thin film at the interface of an HTL and EDT-PbS or I^--PbS for gradient band alignment, achieving a 9.7% PCE. [83] Based on n-type I^--PbS and p-type MPA-PbS CQD-SCs, a hole selective layer (HSL) was introduced at the hole contact side. The HSL prevented electron-hole recombination at the anode and efficiently extracted photogenerated holes, resulting in a 10.23% PCE. Furthermore, a thick HSL layer works as an optical spacer, which enables more light to be absorbed in the active layer. Owing to optical management, CQDs with a V-compound parabolic trapper (enhancing light absorption) exhibited a 11.71% PCE, arising from the improved J_{SC}. [57] Different ligand exchange provides an efficient band alignment structure to realize larger depletion regions and less recombination losses in mixed CQD films. By introducing additional charge selective layers, both the PCE and lifetime of the device could be further improved.

2.1.5 Tandem structure

The layer thickness of CQDs is limited owing to the trade-off between charge extraction and light absorption. The physical parameters of CQDs, such as the charge diffusion length and depletion region, govern the optimal thickness of CQD layers. Hence, advanced structures for utilizing unabsorbed photons due to thin CQD layers are needed. One well-known strategy to convert more photons to electricity is a tandem structure consisting of stacked light-absorbing layers. The most important design factors of tandem cells are E_g tuning between each light-absorbing layer and designing a charge recombination layer between each sub-cell. Prototypes of tandem CQD-SCs, employing 1.0 and 1.6 eV nanocrystals, were reported by Choi et al. [84] The charge recombination layer included ZnO, thin Au (1 nm) and poly(3,4-ethylenedioxythiophene) polystyrene sulfonate (PEDOT:PSS). For efficient energy harvesting, metal oxide layers, such as MoO_3, ITO, AZO, and TiO_2, were adopted in tandem structures as charge recombination layers. The efficient electron-hole recombination at the inter-layer resulted in a 4.21% PCE. [85] However, difficulties in tuning the E_g of CQDs led to the introduction of other types of light-absorbing layers, such as organic layers, to tandem devices. An organic heterojunction light absorber (poly(3-hexylthiophene), P3HT) and [6,6]-phenyl-C61-butyric acid methyl ester (PCBM) were used as the active layer of sub-cells in CQD tandem SCs. An inter-recombination layer with thin Al (1 nm) and WO_3 (15 nm) was used. [86] Further improvement of CQD tandem structures with organic absorbers was achieved by

incorporating the low E_g polymer thieno[3,4-b]thiophene/benzodithiophene (PTB7). Optimization of the inter-layers resulted in a 9.4% PCE. [87, 88] The tandem devices with perovskite SCs were achieved by introducing SnO_2 and PEDOT:PSS as a recombination layer. The E_g tuning of PbS cell led the tuning of V_{OC} which resulted in 11.03% PCE. [89] For all-inorganic devices, the inorganic CdTe nanocrystal was also included in CQD tandem cells. E_g optimization of both PbS and CdTe CQDs with ZnTe and ZnO inter-recombination layers was conducted. [90] EDT-PbS CQDs, Au, PEDOT:PSS and ZnO nanocrystals were used as the charge recombination inter-layer. The downshift of the vacuum energy level arising from the inter-recombination layer allowed the use of the same light-absorbing layer for both sub-cells, achieving an 8.3% PCE. [91] Chemical vapour-deposited graphene and AZO were introduced to the inter-recombination layer, forming efficient PbS CQD-based all-inorganic tandem SCs with an 8.2% PCE as shown in Fig. 6 (a)~(d). [92] Recently, all PbS CQD-based tandem SCs were achieved by introducing graded band alignment. The size of CQDs were precisely controlled and the carrier transport in the charge recombination layer was enhanced, leading to 6.8% PCE. [93]

As we have discussed, the structural development trends of CQD-SCs are extending the depletion region and minimizing the recombination loss of photogenerated charges. An improvement in the materials could enhance the physical characteristics of CQDs, such as the charge diffusion length. However, more space for improving PV efficiencies through structural enhancements remains. Kim et al. suggested a close-packed CQD layer by pressing the film with an external force. [94] Introduction of an ordered structure to CQDs could be a method to overcome the loss of PV parameters. Recently, CQDs were structurally confined with a two-dimensional matrix using lead iodine (PbI_2) and amines (Fig. 6(e) and (f)). [62, 95] A low dimensional device structure induces structural ordering of the CQDs, which significantly reduces their energetic disorder as shown in Fig. 6(g). A possible advantage of ordered CQDs is extension of their intrinsic diffusion, showing efficient charge extraction even for thick CQD layers. The reported high PCE of 12.48% implies that the research direction of structural development of CQD-SCs is promising. Perovskite based CQD-SCs have emerged with phase stability and desirable bandgap. The presents of cubic phase $CsPbI_3$ CQD-SCs boosted the development of perovskite based CQD-SCs. [47] The CQD surface treatment with methyl acetate allowed compact and electrically conductive film state, resulting 10.77% PCE (Fig. 7 (a)~(c)). The bandgap tuning of nanocrystals could be easily achieved by substituting halide ions which makes the application of perovskite based CQDs more feasible for optoelectronic devices. [96] Further improvements on $CsPbI_3$ SCs were reported by cooperating organic perovskite species (formamidinium) or inorganic cesium salts to Cs cation. The larger absorbance range and improved electrical coupling in the active layer improved photovoltaic performances. [54, 66, 97, 98]

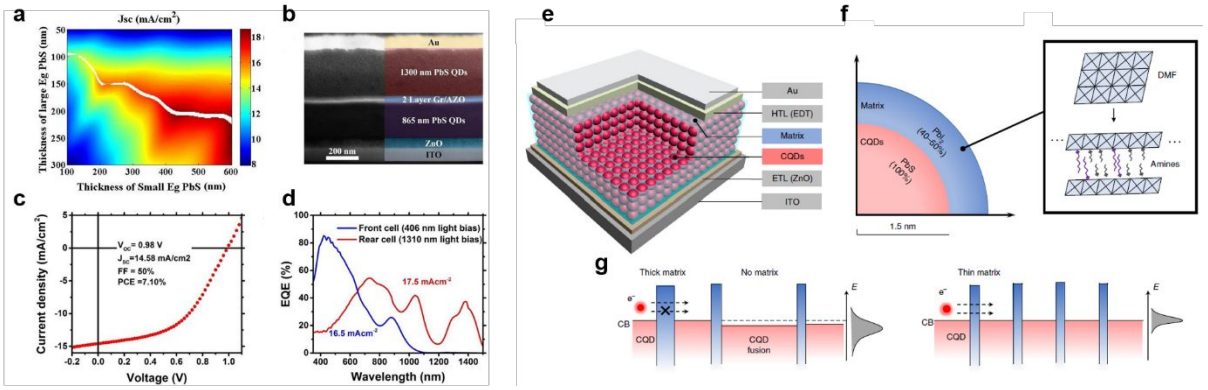

Fig. 6 Tandem and 2D structured CQD-SCs. (a) Simulated achievable J_{SC} in the tandem devices based on the active layer thicknesses. The white lane suggests the optimum thicknesses of each CQD layers. (b) Cross sectional SEM of tandem CQD-SC. (c) *J-V* characteristic of the tandem CQD-SC. (d) EQE of each sub cells of the tandem device. Reproduced permission from ref. [92]. Copyright 2018, American Chemical Society. (e) Schematic diagram of 2D matrix architecture, where CQDs (red) are assembled in a matrix medium (blue). (f) The matrix component is PbI_2. The molecular ratio is about 40~50% compared to PbS which is enough amount to cover a full monolayer. (g) Homogeneity of matrix reduces structural and energetic disorder. The diffusion length and V_{OC} increase with the homogeneity. Reproduced permission from ref. [62]. Copyright 2018, Springer Nature.

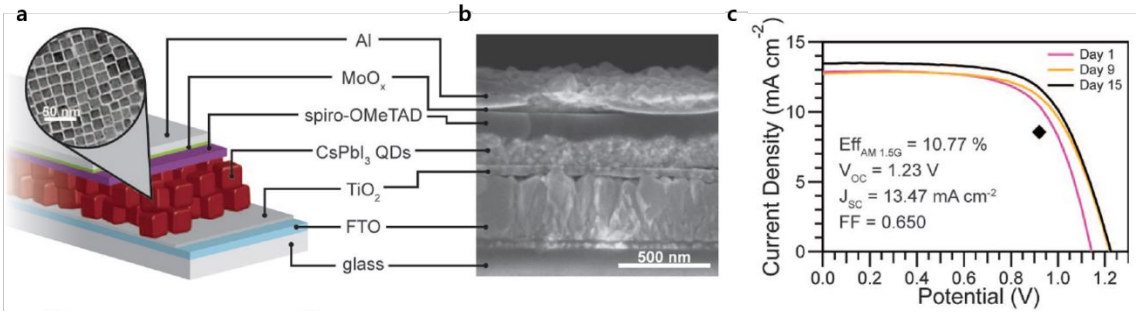

Fig. 7 Perovskite based CQD-SCs. (a) Device structure of $CsPbI_3$ CQD-SCs. (b) Corresponding cross-sectional SEM image. (c) Photovoltaic performance regarding device storage time. The black diamond represents stabilized power output at 0.92 V. Copyright 2016, AAAS.

2.2 Device structure engineering

Understanding the role of each constituent layer of CQD-SCs is essential in optimizing the device efficiency and stability. The charge transport characteristics between each interface play important roles in the device performance. This section covers the device physics for each device constituent layer: CQDs, CTLs and electrical contacts.

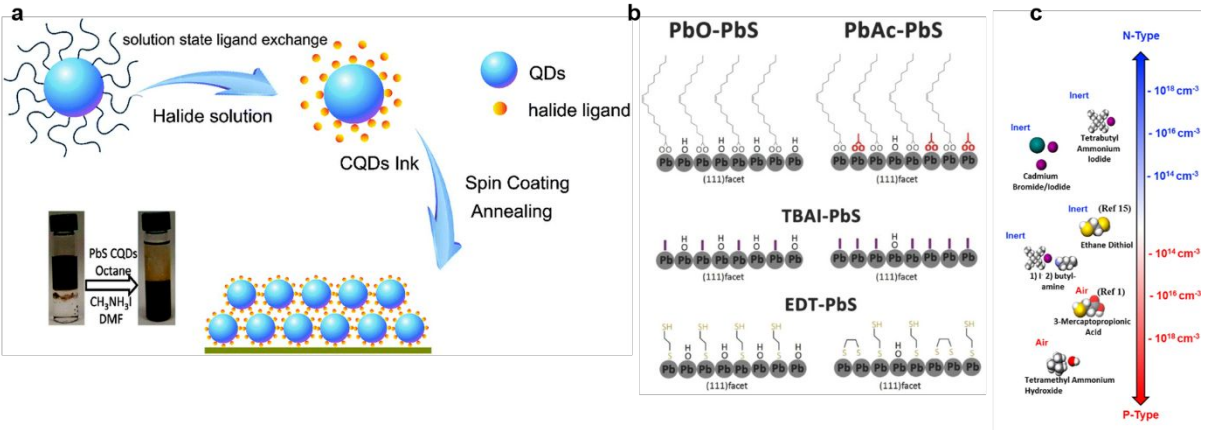

Fig. 8 (a) Schematic diagram of solution phase ligand exchange with halide solution. Long insulating OA chains are efficiently exchanged to short halide ligands. Reproduced permission from ref. [99]. Copyright 2016, The Royal Society of Chemistry. (b) Schematic images of the (111) facet of CQDs from PbO and $PbAc_2 \cdot 3H_2O$ before and after ligand exchange process. Acetate ligands can replace hydroxyl groups during the CQD synthesis. At the final solution,

after ligand exchange, the amount of hydroxyl groups could be significantly reduced by employing acetate ligands. Reproduced permission from ref. [61]. Copyright 2018, Wiley. (c) Doping density variation with the effect of ligand exchange under air or inert conditions. Reproduced permission from ref. [100]. Copyright 2012, American Chemical Society.

2.2.1 Ligand exchange and CQD passivation

Highly concentrated, stable CQD films are essential for the commercialization of SCs made with them. For the stable dispersion of CQDs in organic solvents, long chain ligands, such as oleic acid, have been widely used. [35] These long chain ligands exhibit insulating properties that hinder dot-to-dot carrier transport. If CQDs with long chain ligands are used for the light-absorbing layer in PV devices, the collection efficiency of photogenerated charges would be low. Furthermore, long chain ligands and surface defects of CQDs work as non-radiative recombination centres of photogenerated charge carriers, decreasing the V_{OC} and FF of SCs. Hence, to achieve efficient carrier transfer inside CQD films, improvement of the film conductivity of CQD layers is required, which can be achieved by exchanging long chain ligands with short ones as shown in Fig. 8(a). Ligand exchange shortens the distances between CQDs and increases their packing density, thereby resulting in more efficient charge transport in the CQD film. Even, n-type or p-type CQDs with carrier density variation can be achieved by doping as shown in Fig. 8(c). An atomic ligand with halide ions (I^-, Cl^-, Br^-) can passivate a CQD's defect states and control its energy levels. [27] Ip et al. reported that the mid-gap states of a CQD act as additional electron trap sites for photogenerated electron-hole pairs. [28] Thus, mid-gap trap states are one factor that restricts the PV performance of CQD-SCs. Since the passivation of defect states at CQD surfaces was normally performed in solution rather than in solid films, halide anions were used as passivating materials for the defects. As a result of surface passivation by halide ions, the binding strength between CQDs and ligands was improved, and defects within the bandgap were successfully suppressed. The halide ligand exchange also protected CQDs from oxygen penetration, showing successful synthesis of air-stable n-type CQDs. [38] Additionally, organic short ligands, such as MPA, EDT, and TBAI, have been suggested for improving the electrical characteristics of CQD films. Long insulating oleic acid ligands were exchanged with EDT (p-type) and TBAI (n-type). [35] The successful band alignment of p-type and n-type CQDs employing EDT and TBAI led to efficient carrier transport in the device. Further studies were performed to passivate defect states on the CQD surfaces. Liu et al. reported that organic-inorganic hybrid ligand exchange sharpened the band tails and decreased energy funnelling. [101] The native hydroxyl ligand in CQDs affects the PV performance, so this ligand should be removed or replaced. [44] The passivation of hydroxyl defect states by a hybrid ligand improved the device efficiency and stability. The deep density of traps on the Pb surface could be passivated by I^- doping with a 1.5% I/Pb ratio during the PbS synthesis process. [51] Ligand exchange of pseudohalides, such as thiocyanate anion (SCN^-), was reported to passivate deep trap states at CQD surfaces. [102] The hydroxyl ligands could be partially replaced by introducing lead acetate trihydrate (PbAc) during CQD synthesis. Acetate formed efficient capping ligands with oleic acid, replacing the hydroxyl ligand and enhancing the device performance as shown in Fig. 8(b). [61] Recently, sodium acetate prevented CQDs from aggregating and passivated facet defect states of CQDs.[103] Recent approaches such as UV treatment and oxygen-plasma treatment on CQD surfaces allows reducing density of hydroxyl groups at CQD surfaces and inducing effective p-dope on CQDs. [104, 105]

2.2.2 CTLs

The improvement of materials engineering led to the development of different energy band CQDs. n- or p-type tunability of CQDs by ligand exchange or surface passivation initiated structural development focused on CTLs. The efficient collection of photogenerated charge carriers requires 3 properties: 1) step-wise band alignment between CQDs and CTLs, 2) proper electron-hole mobility balance, and 3) photophysical stability of each layer.

The variation in the optimum conduction band (CB) and VB of CTLs depends on the size of the CQDs, implying that an optimum QD size exists for proper CTLs. As the E_g of a CQD varies depending on the size, CTLs should be carefully chosen considering the energy level of the CQD and its VB and CB. Furthermore, simulation results indicate that the thickness of the CTL plays an important role in balanced charge extraction and electric field redistribution, which is closely related to the maximum J_{SC} in CQD devices. [106] Particularly, the injection dynamics of photogenerated charges from CQD layers to ETLs could be limited by the photoconductivity of the ETLs. [107] To realize efficient charge extraction to an ETL, the photoconductivity of ETLs (mainly TiO_2 or ZnO) and their doping process were widely investigated. Zr or Sb was doped with TiO_2 to achieve higher mobility (0.015 to 0.026 cm^2/Vs). Together with CB tuning of the doped TiO_2, the PV performance was improved. [26] The accumulated carrier density inside the PbS CQD layer was effectively decreased by introducing n-doped PCBM on top of TiO_2. [108] In particular, elemental doping of ZnO led to improved conductivity and better PV performance of the device. Mg doping was performed to induce a band shift of ZnO (Fig. 9(a) and (b)).[109, 110] In addition, In atoms contribute to enhanced light absorption of ZnO-incorporated CQD-SCs by filling vacancy states of the ZnO film and decreasing its parasitic absorption. The CB energy level was tuned by adjusting the In doping concentration to maximize photogenerated charge carrier extraction. [111] Moreover, Cl, Cs, or K was also introduced to dope ZnO, tuning its E_g and energy level. [49, 56, 112] Additionally, surface passivation of ZnO boosts the performance of CQD-SCs with it. The ZnO surface was passivated by WPF-6oxy-F to enhance V_{OC}. The introduction of a surface dipole to the ZnO surface induced a larger Fermi level splitting at the junction. [42] The junction property between CQDs and ZnO was improved by introducing a P(VDF-TrFE) layer. The porous P(VDF-TrFE) exhibited piezoelectric characteristics that generated a converging electric field at the junction.[113] The introduction of three-dimensional graphene network at ETL/CQD junction interfaces reduced fast electron recombination which enhanced charge collection to the electrode. [114] Moreover, the introduction of nanostructured ETLs boosted photovoltaic performance by enhancing charge extraction at the CQD-ETL junctions. The increased interfacial area reduced the trap-related recombination and enhanced bimolecular recombination. The ordered nanopillar structures of TiO_2 enhanced absorbance to photoactive layer suppressing the trap-related recombination. [29] The porous TiO_2 template enhanced increased light absorption with charge de-trapping. [115] Vertical arrays of ZnO nanowires decoupled light absorption from carrier collection at the junction interface, enhancing photovoltaic performance by 35%. [77] Recently, high-performance CQD-SCs were achieved by combining optical management strategies such as ZnO nanowires and energy down shifting CQD optical conversion layers. [116]

In early studies, the structural development of CQD-SCs was focused on forming efficient junctions between CQDs and ETLs because PbS-based CQDs generally exhibit p-type characteristics enabling hole transport through them. Most reports on HTLs have focused on minimizing the energy barrier between CQDs and electrodes and introducing materials that have high hole conductivity for efficient extraction of photogenerated holes. For band

alignment between CQDs and HTLs, CuI was introduced to enable step-wise hole extraction to the electrode. [117] Graphdiyne was inserted between a Au electrode and a CQD layer to reduce charge recombination at the electrode-HTL interface. [45] An organic HSL was applied to passivate a CQD surface. *N,N,N',N'*-tetrakis(4-methoxyphenyl)-benzidine (p-MeO-TPD) efficiently extracted photogenerated holes and blocked drifting electrons, thus decreasing electron-hole recombination at the metal electrode as shown in Fig. 9 (c)~(e). Moreover, regarding the device stability under ambient air, an HSL layer protected CQDs from oxygen penetration. [57] A study on the effect of the HTL's hole mobility revealed that the hole mobility has significant importance, along with the proper energy level alignment with CQDs, indicating that an over 15% PCE could be reached if the high hole mobility (~0.1 cm^2/Vs) and deep HOMO level (~5.4 eV) PTB7 layer could be tuned.[118]

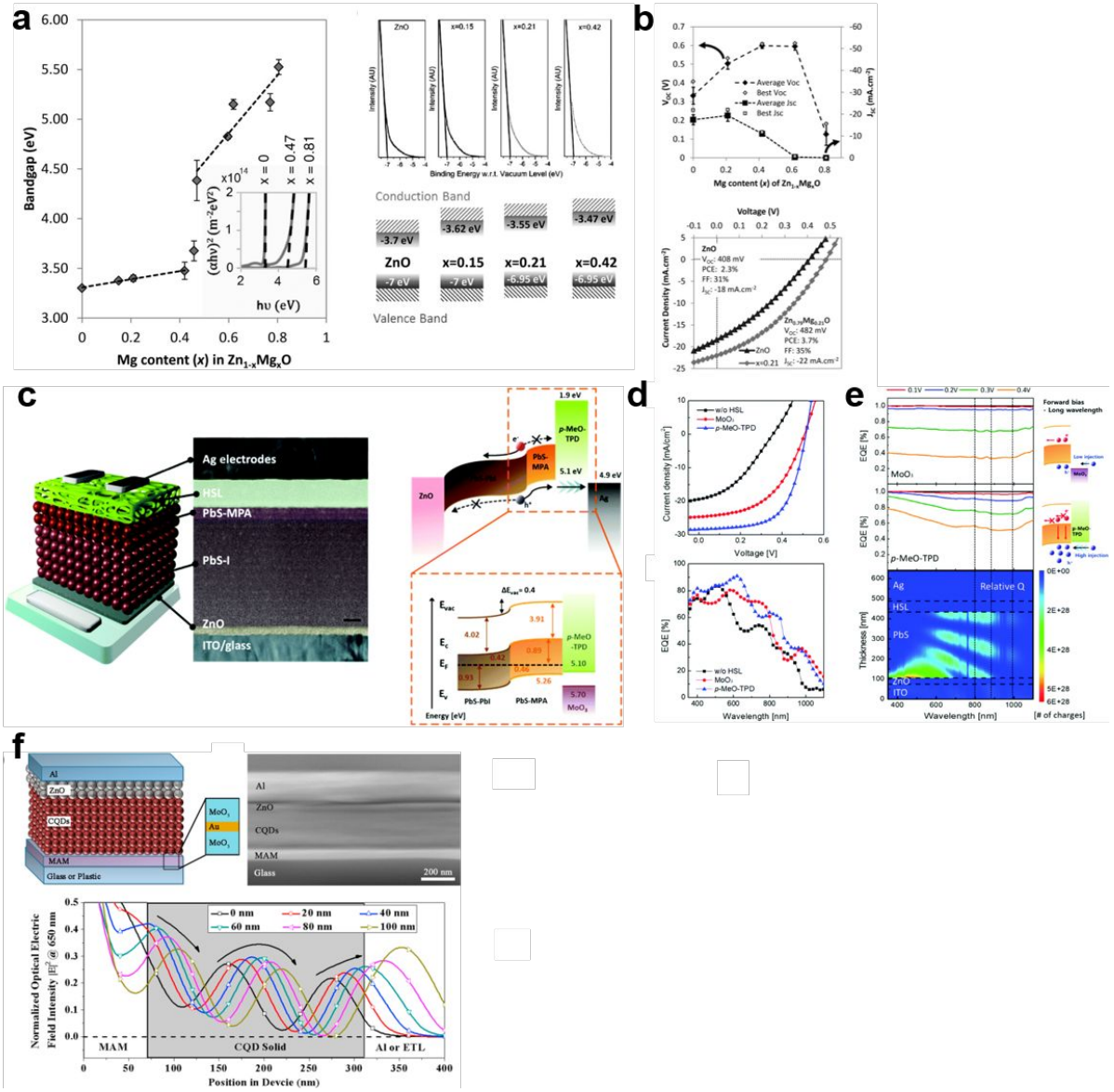

Fig. 9 Device engineering on charge transport layers and metal electrodes. (a) The E_g of ETL (ZnO) tuned by magnesium doping ratio. The valance band of both doped and undoped ZnO layers exhibits no changes. The conduction band edges of doped ZnO are calculated using the UPS data and E_g measurements. (b) The device performances with J_{SC} and V_{OC} variation regarding the magnesium doping effect on ZnO. Reproduced permission from ref. [109].

Copyright 2014, Wiley. (c) Schematic of CQD-SC integrating organic hole selective layer, or HTL. The corresponding energy level alignment of each layers under short circuit condition is depicted. (d) *J-V* characteristics and EQE of the devices with/out HTL. (e) Normalized forward biased EQE of CQD-SCs and the charge generation profiles of the device structures. Reproduced permission from ref. [57]. Copyright 2018, The Royal Society of Chemistry. (f) Schematic of the DMD structured CQD-SC and normalized optical electric field intensity within the device at an incident wavelength of 650 nm. Reproduced permission from ref. [119]. Copyright 2016, Elsevier.

2.2.3 Electrical contacts

The foremost property of electrodes in SCs is matching of the work function to the energy levels of the CTL or CQD layers. As proven for many optoelectronic devices, the formation of an ohmic contact at the electrode is very important. [120, 121] The work function of FTO was tuned to facilitate electron extraction. [33] Shallow work function FTO could be operated with relatively thin ETLs (10 nm). The depletion region was extended by 10%, showing improved PV performance. Work function control of metal counter electrodes has also been widely studied. p-type CQDs require proper band alignment with the work function of metal electrodes. Au electrodes exhibit a higher work function than Al (4.3 eV) and Ag (4.7 eV) electrodes. [25] Then Au reduces the energy barrier with the HTL compared to Al or Ag, which resulted in a lower series resistance of the CQD-SC. Further improvement in the shunt resistance of the devices was achieved by introducing a thin layer of MoO_3. [25, 122] The energy level of the MoO_3 layer was pinned to the VB of CQDs, which lowered the energy level barrier between the CQDs and metal electrodes. Non-radiative recombination at the anode/MoO_3 interface was inhibited, resulting in higher J_{SC} and V_{OC} with higher shunt resistance in the device. When noble Au was replaced with Ni because of its cost-savings and proper work function alignment with the VB of CQDs,[22] sulfur interdiffusion from the CQDs to Ni electrodes deteriorated the PV performance. The introduction of thin LiF efficiently blocked sulfur inter-diffusion, and the photogenerated charges could be extracted to the Ni electrode through a thin tunnelling barrier.

Based on the efficient charge extraction property, metal electrodes and transparent electrodes could be modified to manage light confinement in the light-absorbing layers. Nanostructured diffraction gratings at the ITO surface allowed increased re-absorption of light reflected from the counter metal electrodes. Additionally, the incoming light through the nanostructured ITO was increased. [123] Zhang et al. introduced dielectric-metal-dielectric (DMD) structures to the transparent anode as shown in Fig. 9(f). [119] In the DMD structure, a thin metal layer is sandwiched between each dielectric, such as MoO_3. The DMD structure maximizes the optical transparency by utilizing refractive index matching between the metal and dielectrics. Through optical management, absorption by the anode and re-absorption of the light reflected by the counter metal electrode by the CQDs were maximized. Furthermore, an optical spacer was installed to re-distribute the electric field in the active layer, which provides maximized light absorption at the CQD layers. Additionally, the counter metal electrode could be replaced by DMD structures to realize all-transparent electrodes for CQD-SCs. [124] Recently, semi-transparent CQD-SCs were fabricated by using graphene electrode which shows around 60% transmittance at the 550 nm. [125]

2.3 Carrier multiplication

The Shockley and Queisser limit of the efficiency of single junction PVs is based on the assumption that an absorbed photon generates one electron and hole pair at most. [126] A hot electron excited by high energy (more than two-fold E_g) in a QD has the potential to generate additional electron-hole pairs when it relaxes from a higher energy state to the 1 S_e energy state. The high energy state of hot electrons could be lost via heat, but in some cases, this high energy state additionally excites electrons from the ground state, forming additional electron-hole pairs. The inverse Auger recombination process of hot electrons was reported as carrier multiplication **(**CM**)** or multiple exciton generation (MEG) (Fig. 10(b)). [127, 128] In theory, SCs capable of MEG are expected to overcome the Shockley-Queisser limit. The effects of CM on bulk semiconductor materials and CQDs have been widely compared. [127-135] The materials that have quantum confinement effects, such as CQDs, may slow down hot electron relaxation, [136] and the extra energy from the excitonic transition can be utilized for energy harvesting. Size and structure tuning of CQDs have been widely studied because CM is controlled by the amount of incident photon energy compared to their E_g. [128, 137, 138] In 2009, the first optoelectronic devices that showed over 100% EQE and internal quantum efficiency (IQE) were reported. [139] The photoconductivity at incident photon energy over 2.7 E_g exhibited significant enhancement. This reported CM threshold, 2.7 E_g, exceeded the theoretical calculation by Klimov *et al*. [137] In PbS or PbSe CQDs, the expected threshold for CM was reported as 3 E_g because the effective masses for electrons and holes are similar. The first PVs that utilized CM were reported in 2011 by Semonin et al. [14] As shown in Fig. 10(a), the devices using the 0.72 eV E_g of PbSe CQDs achieved an EQE over 114% and an IQE over 130% under 3 E_g excitation energy. CM could be further enhanced by modifying the CQD structures. PbSe CQD nanorods exhibited a stronger Coulomb matrix than dot structures, which resulted in a 122% EQE and a 150% IQE from 0.8 eV E_g CQD nanorods. [140] However, to date, high power conversion efficiency in CQD-SCs utilizing CM have not been reported. The device structures of CQD-SCs achieved to date may not be ideal for utilizing CM. Moreover, the CM threshold is still high, which needs to be further improved by materials engineering to control the relaxation process of hot electrons.

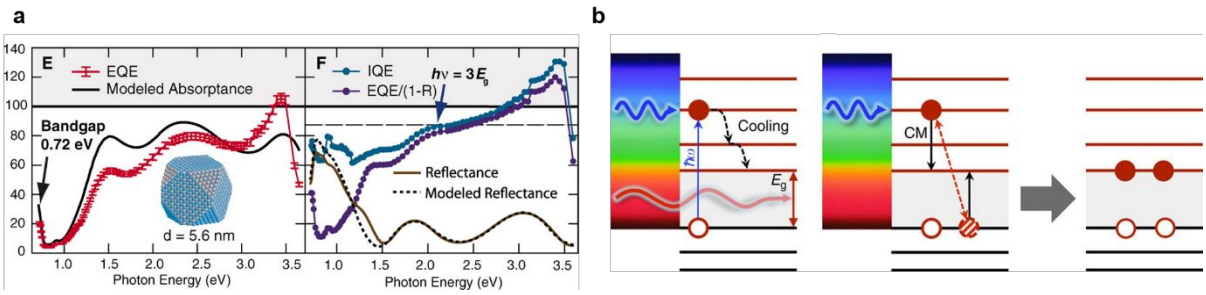

Fig. 10 Carrier multiplication. (a) The measured EQE and IQE over 100% in CQD-SC. IQE begins to rise at a photon energy larger than 3E_g. Reproduced permission from ref. [14]. Copyright 2011, AAAS. (b) Schematic of energy losses in a device from cooling of hot carriers and schematic of CM process. Reproduced permission from ref. [141]. Copyright 2014, Springer Nature.

3. Stability

. As the cost of electricity from SC are determined by its efficiency and lifetime, the levelised cost of electricity (LCOE) is normally calculated by following an equation:

$$\text{LCOE (\$/kWh)} = \frac{\text{total cost of installation and operation (\$)}}{\text{total amount of energy generated by a system (kwh)}}$$

If a photovoltaic system exhibited pre-mature aging, the total amount energy generation from the system would shrink, thereby resulting in higher LCOE. Then the system would lose competitive edge in the market. For instance, the LCEO of device approximately will decrease by half, if its lifetime expands twice. Hence, the stability of SC is a key factor for the commercialization. Unfortunately, the device lifetime, whether the maximum power point tracking lifetime or storage lifetime, is a still bottle-neck for the commercialization of CQD-SCs, in comparison with commercialized c-Si PV system. For example, the commercial c-Si solar panels from market leading companies (Jinko Solar, JA Solar, First Solar, Hanwha Q-cell and most other solar panel manufacturers) have a 25-year warranty for T_{80} (80% of initial efficiency) under standard test conditions (1000 W/m^2, AM 1.5 G, 25°C). And they also guarantee that the initial drop of their product is less than 4% within 1 year. [142] Since the device stability has been the most limiting factor for the commercialization of CQD-SCs, it has been continuously investigated and enhanced. Table 2 shows the development of the device stability with respect to the device structure, measurement condition and publication year. The stability of CQD-SCs exceeds 1100 hours (T_{80}, under illumination) and has been increasing. The stability merit could be an intuitive tool for comparing the stabilities of CQD-SCs to those of commercialized c-Si SCs (Fig. 11). The stability merit represents the importance of the stability as well as PCE of the devices. Although a large gap still exists between c-Si SCs (green dashed line in Fig. 11) and CQD-SCs, much room for extending the device lifetime of CQD-SCs by improving materials or through device engineering remains. In this section, we will discuss the effects of the most common device degradation sources and the strategies for overcoming these device degradation processes.

Table 2. Stability table of CQD-SCs.

Device type	Device structure	Measurement condition (dark)	Measurement condition (illumination)	Device stability (dark)	Device stability (illumination)	PCE	Stability merit (dark)	Stability merit (illumination)	Published year	Ref
Schottky	ITO/PbS/LiF/Al/Ag	Ambient air storage	-	60% at 160 hours	-	2%	1.2	-	2010	71
Depleted heterojunction	ITO/ZnO/PbS/Au	-	0.7 sun illumination	-	90% at 1000 hours	2.94%	-	2.65	2010	21
Depleted heterojunction	ITO/PbS/PbS-Ag/AZO/Ag	-	MPP (encapsulated)	-	90% at 60 hours	6.1%	-	5.49	2012	30
Schottky	ITO/PbS/LiF/Al/Ag	Ambient air storage	-	55% at 500 hours	-	3.39%	1.86	-	2014	70
Schottky	FTO/PEI/PbS/MoO_3/Au-Ag	Ambient air storage	-	70% at 450 hours	-	3.8%	2.66	-	2014	72
Band alignment	ITO/ZnO/PbS-TBAI/PbS-EDT/MoO_3/Au	Ambient air storage	-	99% at 150 days	-	8.55%	8.46	-	2014	35
Band alignment	FTO/TiO_2/PbSe-PbI_2/PbSe-MPA/Au	Ambient air storage	-	99% at 60 days	-	6.47%	6.41	-	2015	143
Depleted heterojunction	FTO/ZnO/TiO_2/PbS/Au	Ambient air storage	-	99% at 130 days	-	6.13%	6.07	-	2015	144

Device type	Device structure	Measurement condition (dark)	Measurement condition (illumination)	Device stability (dark)	Device stability (illumination)	PCE	Stability merit (dark)	Stability merit (illumination)	Published year	Ref
Depleted heterojunction	FTO/TiO_2/PbSe/Au	Ambient air storage	1 sun illumination	75% at 2000 hours	70% at 3.5 hours	3.5%	2.63	2.45	2016	145
Band alignment	ITO/ZnO/PbS-I/PbS-EDT/Au	Nitrogen storage	1 sun illumination (nitrogen)	97% at 30 days	80% at 1100 hours	9.6%	9.31	7.68	2016	44
Band alignment	ITO/ZnO/PbS-TBAI/PbS-EDT/GD/Au	Ambient air storage	-	95% at 120 days	-	10.64%	10.11	-	2016	45
Band alignment	FTO/TiO_2/$CsPbI_3$/Spiro-OMeTAD/MoO_x/Al	Desiccator	-	100% at 64 days	-	10.77%	10.77	-	2016	47
Band alignment	ITO/ZnO/PbS (PbX_2/AA)/PbS-EDT/Au	Ambient air storage	-	90% at 1000 hours	-	11.28%	10.15	-	2017	101
Band alignment	ITO/IZO/PbS-TBAI/PbS-EDT/Au/TeO_2	Ambient air storage	MPP	95% at 70 days	90% at 0.9 hour	7.3%	6.94	6.57	2017	146
Band alignment	ITO/ZnO-SAM/PbS-PDMII/PbS-PDT/Au	Ambient air storage	MPP	95% at 24 days	97% at 4.5 hours	10.89%	10.35	10.56	2017	48
Band alignment	ITO/MZO/PbS-TBAI/PbS-EDT/Au	Ambient air storage	MPP	90% at 103 days	95% at 1 hour	10.4%	9.36	9.88	2017	53
Quantum junction	ITO/ZnO/n-PbS/p-PbS/Au	Ambient air storage	-	80% at 100 days	-	10.94%	8.75	-	2018	55

Device type	Device structure	Measurement condition (dark)	Measurement condition (illumination)	Device stability (dark)	Device stability (illumination)	PCE	Stability merit (dark)	Stability merit (illumina	Published year	Ref
Band alignment	ITO/ZnO/PbS-I/PbS-MPA/HSL/Au	Ambient air storage	-	90% at 180 days	-	11.71%	10.54	-	2018	57
Band alignment	ITO/ZnO-K/ PbS-I/PbS-PDT/Au	Ambient air storage	1 sun illumination	95% at 90 days	95% at 10 hours	10.8%	10.26	10.26	2018	56
Band alignment	ITO/ZnO/PbS-PbI_2/PbS-EDT/Au	Ambient air storage	-	70% at 365 days	-	11%	7.7	-	2018	2
Band alignment	ITO/MZO/PbS-PbX_2/PbS-EDT/Au/MgF_2	Ambient air storage	1 sun illumination (white LED)	99% at 103 days	85% at 540 hours	8.4%	8.32	7.14	2018	147
Band alignment	ITO/MZO/PbS-$CsPbI_3$/PbS-EDT/Au	Ambient air storage	MPP	99% at 43 days	88% at 46 hours	10.5%	10.4	9.24	2018	148
Band alignment	ITO/CsZnO/PbS-TBAI/PbS-EDT/Au	Ambient air storage	-	97% at 90 days	-	10.43%	10.12	-	2018	112
Band alignment	ITO/ZnO/PbSe-PbI_2/PbS-EDT/Au	Ambient air storage	-	94% at 1000 hours	-	10.68%	10.04	-	2019	149
Band alignment	ITO/PTAA/$CsPbI_3$/C60/BCP/Graphene	Ambient air storage (20% RH)	-	96% at 14 days	-	5.11%	4.91	-	2019	125
Band alignment	ITO/ZnO/PbS-TBAI/PbS-EDT/Au	Ambient air storage (50% RH)	-	90% at 90 days	-	8.9%	8.01		2019	105
Band alignment	ITO/ZnO/PbS-TBAI/PbS-EDT/Au	-	1 sun illumination (N_2)	-	96% at 230 hours	10.6%	-	10.18	2019	104

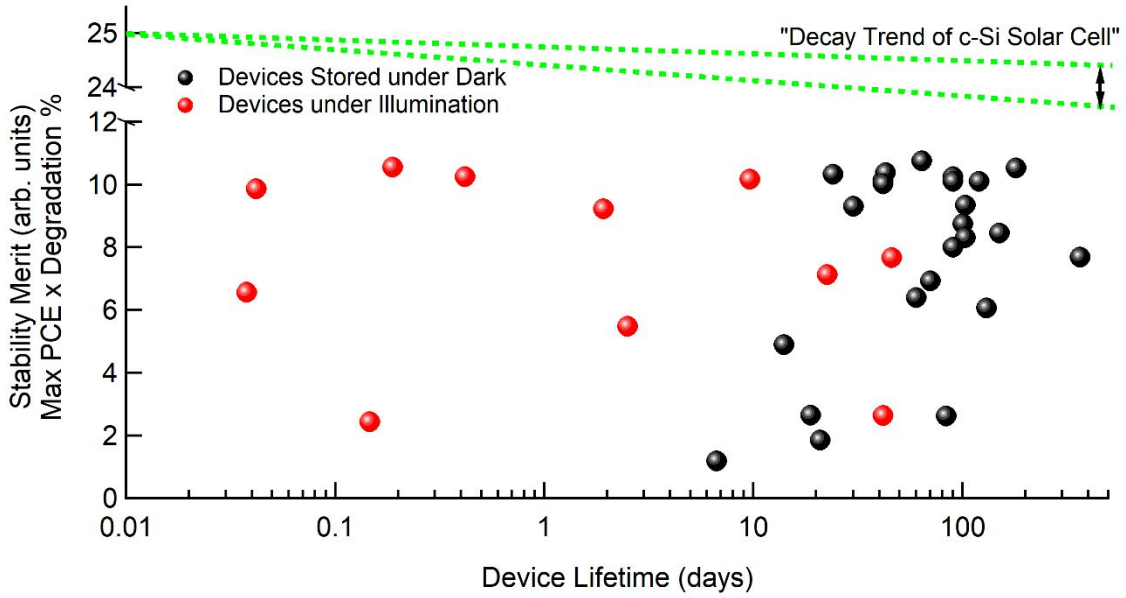

Fig. 11 Stability Merits regarding device lifetime of CQD solar cells compare to commercial c-Si solar cell. Stability merits are calculated by multiplying maximum PCE and corresponding device degradation percentage. For example, the stability merit of CQD-SC which exhibits 10% maximum PCE and T_{80} (time for PCE decrease to 80% of initial value) at 100 days could be calculated as 10 x 0.8 = 8. Green dashed line represents decay trend of commercial c-Si solar cell. Here, the line is assumed that the drop rate of c-Si SC is around 2-4% (relative) in the first year of operation. [142] Black and red dots are stability merits of CQD-SCs under dark and illumination condition, respectively. All the plotted data is based on the table 2.

3.1 Degradation mechanisms

Oxygen and humidity degradation

When Pb-based CQDs react with ambient air, lead sulfite ($PbSO_3^{2-}$) or sulfate ($PbSO_4^{2-}$) could form on their surfaces (Fig. 12(a) and (b)).[150, 151] $PbSO_3^{2-}$ has been reported to create shallow trap states (depth ~0.1 eV), while $PbSO_4^{2-}$ generates mid-gap trap states (depth ~0.3 eV) around the CB of CQDs, which are critical for device performance and stability. Larger CQDs are prone to exposure to oxygen from air, exhibiting more $PbSO_4^{2-}$ components than smaller CQDs after degradation. Moreover, volume shrinkage (~ 50%) of a CQD solution was reported when the solution was exposed to air. The 50% CQD solution was transformed to lead oxide components within 24 hours. The effective core size of the CQDs decreased, enhancing the quantum confinement effect and causing a PL band shift. [152] The optoelectronic application of CQDs requires ligand exchange processes, as discussed in section 2.2.1. During the ligand exchange process, detached sites of long ligands could remain as empty sites without further short ligand attachment. Oxygen could become attached to such an empty site, acting as a defect state. This oxygen-induced quenching site provides additional trap states for photogenerated charge carriers, thus decreasing the PV performance and stability. In particular, both the non-polar (100) and polar (111) facets of Pb-based CQDs are easily exposed to oxygen and thus require passivation. [153] Kirmani et al. reported that the device performance would be degraded when the devices are fabricated under high humidity or non-humidity-controlled conditions. [2] Downshifting of a p-type CQD's Fermi level via oxygen doping could enhance

hole extraction, with reduced non-radiative recombination. However, a high humid environment inhibits effective oxygen doping of EDT ligand-based CQDs. Thus, effective oxygen doping of p-type CQDs could be achieved by storing PV devices under dry air conditions. The degraded device, fabricated under high humidity, could be recovered by storing it in a dry atmosphere. Once the device performances had recovered, the devices exhibited a high stability under humid conditions. The dry-air-stored devices followed the same decay trend as the PV devices fabricated under dry air conditions.

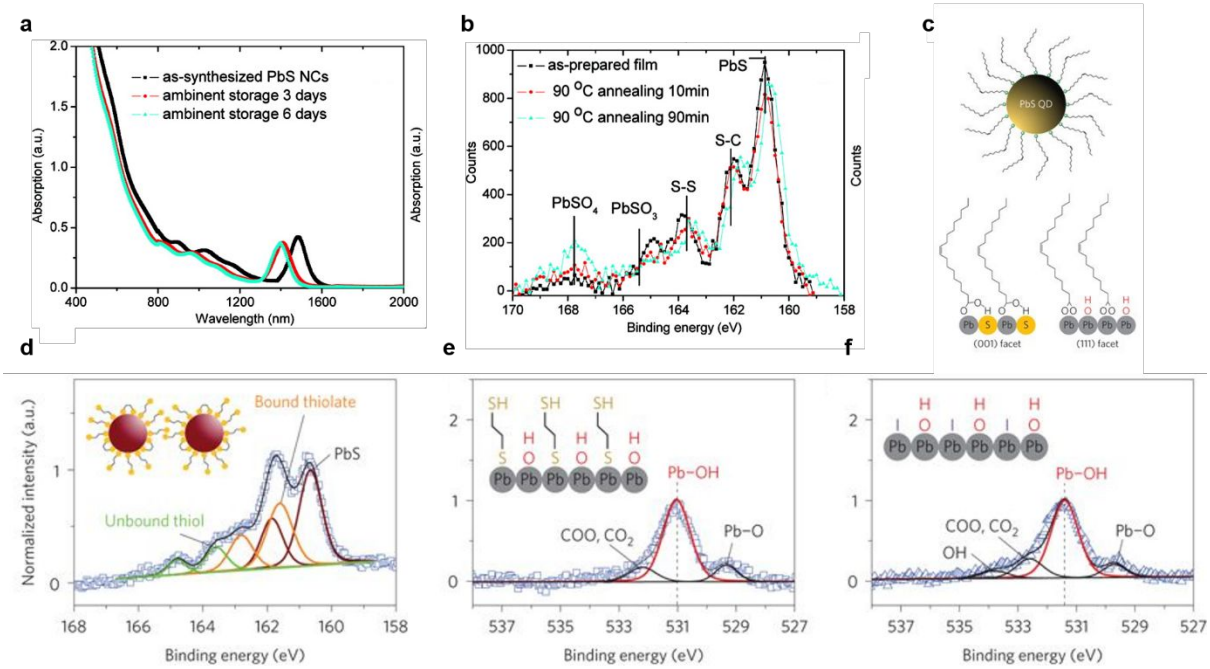

Fig. 12 Degradation sources of CQDs. (a, b) Comparison of oxidation characteristics with absorbance and X-ray photoelectron spectroscopy (XPS). The absorbance peak shifts by CQD oxidation. The thermal degradation results increasing lead sulfate formation. Reproduced permission from ref. [150]. Copyright 2010, American Chemical Society. (c) Schematic figures of CQD with oleic surfactants showing (111) facet is occupied with hydroxyl groups. (d) XPS S 2p signals exhibit lead sulfite and sulfate formation on CQD surfaces. (e, f) XPS O 1s signals from EDT and TBAI ligand exchanged CQDs. Hydroxyl groups are still detected after ligand exchange process. Reproduced permission from ref. [44]. Copyright 2016, Springer Nature.

Light-induced degradation

The hydroxides on CQD surfaces have been reported to be unstable under light exposure. [154-156] The most widely used ligand exchange processes with EDT and TBAI were reported to lead to hydroxide species on the Pb-terminated (111) surface facets as shown in Fig. 12(c)~(f). [44] These hydroxide sites exhibited quenching of photogenerated electrons and holes, thus increasing the non-radiative recombination rate, which is critical for the device stability under illumination. Additionally, the most widely used ETL for record high-efficiency CQD-SCs is ZnO. Thus, investigation of the light stability of ZnO is worthwhile. Several reports on the photostability of intrinsic and modified ZnO have been presented, [48, 56] and degradation of the ZnO interface or ZnO itself under illumination is expected. The sensitivity of ZnO or its light soaking behaviour under illumination has been reported for various types of SCs. Kim et al. reported that the ZnO layer was degraded under 1-sun illumination, causing increased energetic

disorder around the CB edge. [157] Additional trap states were created, resulting in decreased V_{OC}. Furthermore, oxygen-containing defects on the ZnO surfaces have been reported to cause inferior photostability.[158-160]

Some CQD-SCs exhibited interesting decay trends under illumination. The degraded PCEs recovered to their original level or higher after storing the devices under dark conditions. [147, 148] This self-healing process was also reported in perovskite SCs. [161] The light-activated meta-stable trap states can accumulate under light illumination. The charged region in the bulk leads to degradation of the photocurrent. When the devices are kept in the dark state, these paths disappear, and the efficiency recovers. The degradation mechanism under light illumination should be considered as the combined effect of defect states on the CQD surfaces and in the interlayers of the device.

Thermal degradation

The formation of lead sulfite or sulfate at the CQD surface can be accelerated at elevated temperatures. [150] The CQD films annealed at 90°C for 10 min showed increases in the oxygen composition from 6% to 9% depending on the CQD size. The XPS S 2p spectra of annealed CQDs implied that the amounts of both lead sulfite and sulfate were increased by applying heat as shown in Fig. 12(b). The increased lead sulfite and sulfate amounts induced additional trap states lying below the CB of the CQDs (0.1 and 0.3 eV for sulfite and sulfate), which cause degradation of charge extraction in SC applications. The thermal stability of ZnO, as investigated in the light degradation section, should contribute to the overall thermal device degradation. The thermal degradation effect in CQD devices was investigated in terms of the effect of AZO. [30] The device stability was very good for 3 hours at 90°C. The interfacial robustness arising from the AZO inhibited the formation of lead sulfate when the devices were heated. This result implies that a robust capping layer on the CQDs can effectively mitigate oxygen penetration, thus diminishing the oxygen-induced thermal degradation. Thus, when the degradation study of CQD films is extended to devices, the effect of the thermal degradation of adjacent buffer layers should also be investigated. The inorganic parts in typical CQD-SCs, such as ZnO, TiO_2, and CQDs, can be considered to be stable at high temperatures. However, recent reports have introduced additional organic HTLs to realize efficient hole extraction, which can be considered unstable under high-temperature environments. [57, 78, 118] Thus, more systematic investigation on the thermal stability of advanced device structures with high PV performances should be performed.

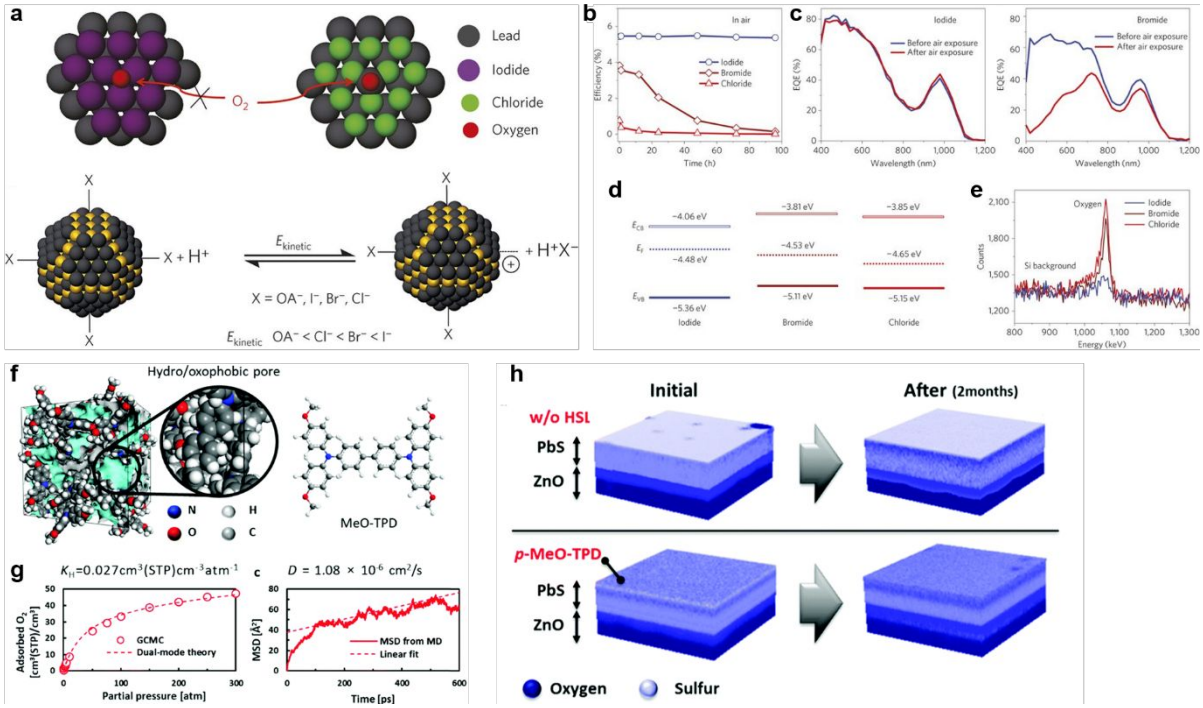

Fig. 13 Strategies to improve stability of CQDs. (a) Iodide ligand exchange successfully passivate the dangling bonds on CQD surfaces inhibit oxygen penetration. The origin of iodide-ligand based defect passivation comes from the high reaction kinetic energy of iodide. (b) PCE comparison between different halide ligand exchange processes. Iodide ligand exchanged device showed much higher stability over other halide ligand used devices. (c) Iodide-processed CQD-SC shows no EQE difference before and after air exposure. Bromide-processed CQD film was oxidized after exposed to air, resulting significantly reduced EQE after air exposure to device. (d) Iodide ligand exchanged CQD film maintains n-type characteristics whereas other halide-processed CQD films become p-type following oxidation. (e) Rutherford backscattering spectrometry confirms that iodide-processed CQDs are resistive at oxidation. Reproduced permission from ref. [38]. Copyright 2014, Springer Nature. (f) Schematic of hydro/oxophobic pore structured HTL. (g) The oxygen permeability as a function of partial pressure and the diffusion constant of entrapped oxygen from MD simulations. (h) The 3D depth profiling of TOF-SIMS. Reproduced permission from ref. [57]. Copyright 2018, The Royal Society of Chemistry.

3.2 Strategies to improve device lifetime

Many studies on passivating degradation sources have been reported, as discussed in the previous section. To prevent dangling bonds created by oxygen penetration into CQDs, several strategies, such as ligand exchange or surface chemistry modification, have been developed. The packing density (higher stability) of CQDs was increased by a factor of two through the ligand exchange process with n-alkylthiolate compared to the tert-butylthiolate ligand exchange process. [162] Halide species (I^-, Br^-, Cl^-)-capped CQDs were robust under oxygen exposure. [38, 44, 101, 145, 148] Mostly, the iodide complexes showed better stability than bromides or chlorides as shown in Fig. 13(a)~(e). The cation exchange from ZnSe using halides (PbX_2, X=I, Br, or Cl) allows CQDs to withstand oxygen and humidity. [143] In addition, shell structures were introduced to produce CQDs with core/shell structures and enhance the CQD stability.

[163, 164] The undesirable oxidation of PbS CQDs was inversely utilized to enhance the CQD stability. [70] The amounts of lead sulfite and sulfate were increased by PbS oxidization, but the partial oxidization of PbS surfaces induced efficient Fermi level pinning between the electrode and CQDs, which raised the Schottky barrier and enhanced the light stability. A thin LiF layer was introduced between PbS and Al electrodes to prevent oxygen and moisture penetration. The delayed oxidization of both the PbS and Al electrodes made the device more stable. [71] The light-unstable hydroxide species could be replaced with photostable alkyl-terminated ligands, such as an oleic surfactant, which resulted in enhanced light stability.[165]

The most commonly used ETL, ZnO, was modified to passivate the unfavourable defect states on the surfaces. The thermal robustness of the entire device was enhanced by introducing aluminium dopants into ZnO. [30] Magnesium- and cesium-doped ZnO also exhibited enhanced robustness, with enhanced stability of the SCs. [53, 112] Potassium-doped ZnO showed enhanced light stability. [56] Deposition of a thin layer of TiO_2 on a ZnO layer led to enhanced stability. [144] Self-assembled monolayer (SAM) treatment of the ZnO layer made the device more robust. [48]

Further stability enhancement was achieved by introducing an HTL passivation layer over the CQD layers. Single-walled carbon nanotubes were introduced as an additional hole extraction layer that significantly enhanced the shelf-life and light stability of the device. [166] Organic HTLs were introduced to prevent oxygen and sulfur diffusion, resulting in stability enhancement (Fig. 13(f)~(h)).[57]

Inorganic encapsulation-like strategies for achieving higher stability were also reported. A stack of inorganic thin films has proven to make devices more stable, which is valid in CQD-SCs. [167] A TeO_2 capping layer was deposited on a full device, which effectively prevented the penetration of oxygen and humidity. [146] Similarly, an MgF_2 capping layer was deposited on a full device, resulting in a significant enhancement of the device stability. [147]

The shelf-life of CQD-SCs have been continuously investigated and improved, exhibiting high stability over 5 months. [35] However, the device stability under illumination conditions is insufficient and needs to be improved. The photostability of devices could be improved by understanding the interaction mechanisms between CQDs and adjacent interlayers. To date, many photostability-related reports regarding ZnO modification have been presented, as discussed in this section. These reports imply that much room remains in improving ZnO to realize a higher photostability. Moreover, eventually, a light-robust ETL or an improved CQD-SC structure will be needed.

4. Manufacturing

4.1 CQD film formation

Transformation of CQD solutions to solid films is key to demonstrating QD-based optoelectronic devices. Since the absorption of incident photons is one of the main determining factors of the efficiency of QD-SCs, the formation of a thick and uniform CQD film through various solution-based methods has been extensively studied. In addition, recombination losses must be minimized and charge extraction to the electrodes must be optimized. For instance, the mean distance between dots should be minimized to enhance the electrical properties of CQD-SCs. [94, 168, 169] As mentioned in Section 2, short ligands are widely adopted to the CQD surface to realize preferential transport of photo-generated carriers. Regarding these factors, three major solution-based approaches, drop casting, spin coating, and dipping method, have been mainly employed in CQD-SC fabrication on the lab scale (Fig. 14). In this chapter, the progress in the film fabrication methods, including strategies for realizing large-area films, is presented.

Table 3. Comparison of different deposition techniques for CQD-SCs.

Methods	CQD consumption	Thickness control	Process Speed	Examples of reported PCE	Ref
Spin coating	Very high	Good	Low	13.4% ($CsPbI_3$)	54
Dip coating	High	Good	Low	10.6% (PbS)	58
Drop casting	Moderate	Poor	Moderate	2.1 % (PbS)	170
Inkjet printing	Low	Good	High	-[c)]	
Spray coating	Low or moderate[a)]	Moderate or Poor	High	8.1% (PbS)	171
Doctor blade coating	Low	Good	High[b)]	10.0-10.3% (PbS)[d)]	2, 55
Slot-die coating	Low	Good	High		

a) Depending on the spray system, the consumption may be varied

b) According to polymer solar cell result, the speed of doctor blade approach is around 15 mm/s

c) Inkjet based CQDSCs have been barely reported.

d) CQD ink for doctor blade coating can be compatible with slot-die method without further modification.

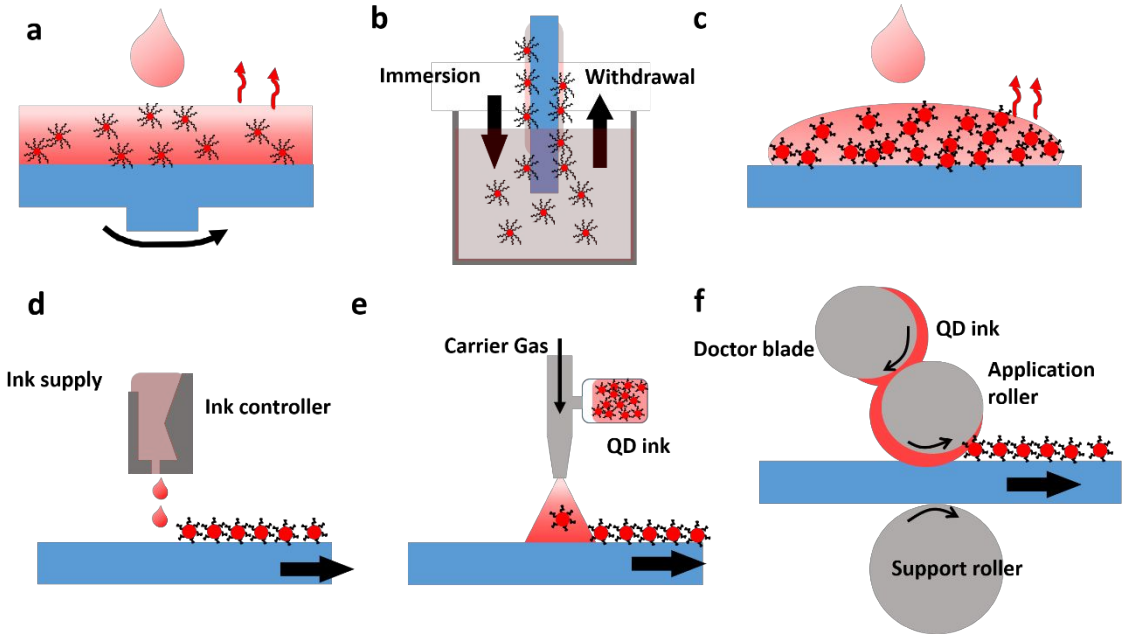

Fig. 14 Various coating method for CQD SCs: (a) Spin-coating, (b) dip coating, (c) drop casting, (d) Inkjet printing, (e) Spray coating, and (f) doctor-blade coating. The long ligand encapsulating CQD can be substituted to short one through post-deposition treatment in spin and dip casted film. On the other hand, pre-treated CQD ink with short ligand is widely used in drop-casting, Spray coating, Inkjet coating, and doctor blade methods.

4.1.1 Drop casting

Drop casting is the simplest method for forming lab-scale small-sized solid QD films. A liquid solution drop is spread over the target area, and the solvent completely evaporates. Compared with other solution-based film formation methods, the drop casting process is very simple yet good for decreasing material waste. In addition, solvent engineering of the CQD solution enables the formation of a thick film with a single drop. Fischer et al. successfully developed stable CQD ink and demonstrated CQD-SCs employing the drop casting method. [170] Here, 1-thioglycerol-capped PbS QDs were well preserved in dimethyl sulfoxide (DMSO) solvent with a pH-adjusting agent. Well-dispersed CQDs in solvent allow fabrication of thick CQD films using the drop casting method. According to the study, the consumption of materials for forming a CQD film significantly decreased (1/40) in the drop casting method (0.88 g/m^2) compared to the layer-by-layer coating method (38.75 g/m^2) as shown in Fig. 15. Moreover, a 200 nm QD film was achieved by a single drop casting process in this work. Despite simple processes with reduced material consumption, the drop-cast devices have shown limited PV performance because of their poor film conditions induced by the non-uniform evaporation of the solvent and non-controllable nanomorphology of the active layer. [52, 172] As a result, possible solvents for CQD synthesis are limited, and the use of additives for dispersion is inevitable in the drop casting approach. [170, 173]

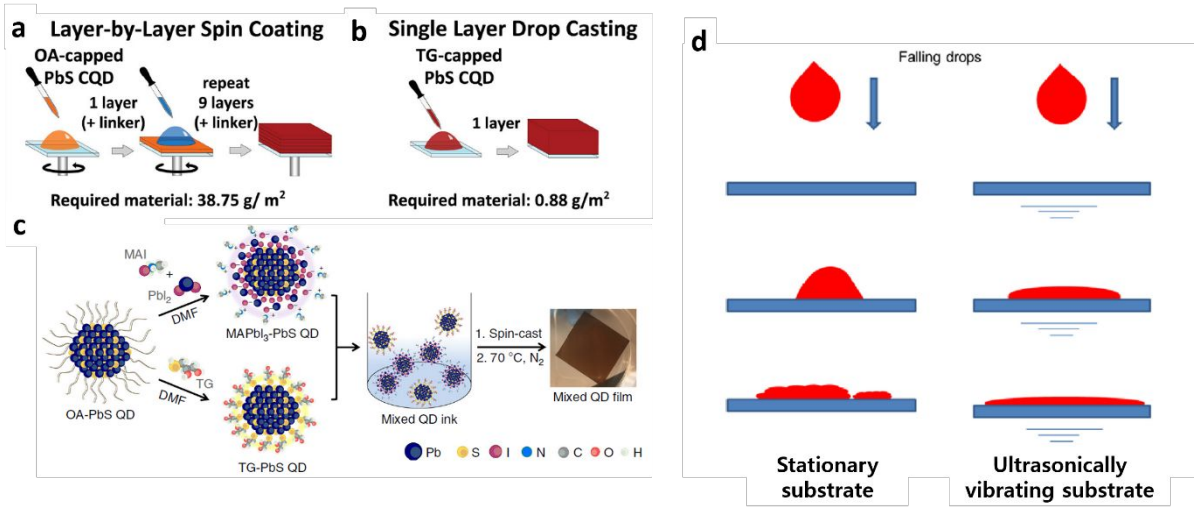

Fig. 15 (a) and (b) Comparison of CQD ink consumption for thick film through spin coating and drop casting. Here, thioglycerol (TG) and oleic acid (OA) were used for dispersing CQD in solvents. Reproduced permission from ref. [170]. Copyright 2013, Wiley. (c) pre-mixed CQD ink capped by TG and methylammonium lead triiodide ($MAPBI_3$). The pre-mixed ink enables us to control carrier transport in CQD film by modifying nano morphology of film. Reproduced permission from ref. [52]. Copyright 2017, Springer Nature. (d)Ultrasonic Substrate vibration-assisted drop casting for the fabrication of solution processed light harnessing semiconductors. Reproduced permission from ref. [174]. Copyright 2015, Springer.

To achieve better film quality and superior performance of the device, several modifications of the drop casting method have been conducted. With the assistance of substrate vibration, the morphology of the CQD films could be smoother, as proven in perovskite films and SCs. [174] Additionally, control of the mixing ratio between PbS QDs capped by different ligands improved the carrier transport balance in the drop-cast film, as shown in Fig 15. [52] It was found that the miscibility among CQDs capped with different ligands affects the carrier extraction balance. Although the reported PCE of drop casted CQD SC is very low (2.1%) currently, basic studies about ink preparation and film formation for drop-casted CQD layers will provide a valuable guideline for mass production of CQD SCs based on simple, high-throughput processes.

4.1.2 Spin and dip coating

Spin and dip coating methods are mostly adopted in CQD-SC research since they are good for small-scale and batch-driven films. In the spin coating method, a CQD solvent is spread on a glass or flexible substrate and changes into a thin film through the high-speed rotation of the substrate. While the substrate rotates, the low-boiling solvent evaporates, and the solid QD film is cast (Fig. 14 (a)). In contrast, in the dip coating approach, the substrate is immersed into a CQD solution. By dipping and withdrawing the substrate, a thin layer of QDs is deposited on the target substrate, whereas the solvent evaporates.[21, 175] In comparison to the spin-coated film, the material consumption is significantly reduced for the dip-coated film. Since the size of the equipment for spin and dip coating is sufficiently small to fit in an inert-gas-filled glove box

and/or closed system, these approaches are suitable for evaluating the full potential of materials by isolating CQD films from oxygen or humidity. [71, 176, 177] As these approaches are also less dependent on the solvent than drop casting, CQD-SCs have been developed using various solvents, including toluene, dimethylformamide (DMF), hexane, and so on. [46, 178] Moreover, the attainable advantage of the spin and dip coating methods is the easy tunability of the thickness of the deposited film by controlling the number of repeated processes, which may be considered a type of layer-by-layer (LBL) deposition. [39, 71, 175, 179] Furthermore, LBL-based coating and dipping methods are very suitable for exchanging long ligands passivating CQDs with short ones during the process. To maintain a uniform distribution of CQDs and suppress their aggregation in the solution state, CQDs are normally capped with long ligands, such as oleic acid (OA). However, this long ligand acts as a barrier for charge transport among QDs. [168, 180, 181] Thus, the inter-dot distance must be decreased to improve the performance of CQD-SCs. As a physical approach, external pressure can be used to compact the QD active layer by removing voids, which results in improved carrier transport and device performance.[94] In contrast, in chemical ligand exchange approaches, long ligands are substituted by short ligands after the surface modification and washing steps of the LBL process. Depending on the polarity of the exchanged ligand, the carrier transport inside the film can be controlled. [11] In particular, PbS or PbSe CQDs can form either an n-type or p-type active layer by introducing TBAI and EDT ligands, respectively. [27, 35, 44, 99] By introducing different short ligands during the modification step of the LBL process, a p-n structure active layer can be utilized with the same set of CQDs, which enables directional control of the photogenerated carrier. In addition, a mild washing solvent (e.g., acetonitrile) reduces the defects on the QD surface during the LBL washing process, thereby resulting in reduced recombination losses and higher device performance. [36, 60] As a result of these developments, record-breaking efficiencies have been reported mainly in devices using the spin and dip coating approaches. [18, 54]

4.2 Upscaling methods

While many solution-based approaches for CQD-SCs have been successfully developed, most of them have been conducted with small-sized substrates using lab-scale systems. Unfortunately, uniformity and sufficient thickness over a large area are difficult to achieve using these film formation techniques. Reduction of material consumption is a big challenge for dip- and spin-coating approaches. LBL-based thick films are not suitable for mass production due to the lengthy process consisting of multiple deposition and washing steps. Additionally, the drop casting method requires careful handling of the solvent to achieve uniform films. Thus, a single-step deposition method in which the thickness and uniformity of QD films can be controlled is desirable for mass production. For example, a Canadian CQD-SC company, the QD solar Inc., have focused on forming QD films from a single step method for fabricating device through roll-to-roll process. By employing pre-ligand-exchanged CQD inks, thick and uniform QD films have been demonstrated despite several challenges, such as poor colloidal stability, use of high-boiling-point solvents for CQD dispersion, and so on.[52, 182] [171] Three common single-step approaches for constructing QD-based optoelectronic devices are inkjet printing, spray coating, and slot-die coating, as shown in Fig 14. The properties of each method are summarized and compared to those of lab-scale processes in Table 3. The advantage of these approaches is the ability to fabricate devices with reduced material consumption in a short time. The current status of each deposition method will be addressed.

An inkjet printing system deposits expensive materials with reduced material consumption over a target area. Thus, this method is widely used for solution-based electrically functional

materials. Using multiple nozzle heads, which cover the entire substrate, a large-area film can be easily deposited within a certain time. Moreover, the film uniformity can be controlled by modifying the solvents. However, the coffee-ring effect caused by the uneven evaporation rate of the solvent in the ink deteriorates the uniform performance of CQD-SCs. The introduction of a mixed solvent for QDs led to reduced surface tension and viscosity, which enables the fabrication of reproducible flat films. [183] Many inkjet-based PV devices have been developed because of their excellent film quality and acceptable film deposition process for large-size films. [184-186] However, to date, most studies on inkjet-printed CQD optoelectronic devices have focused on LEDs rather than PV cells since complicated patterned light-emitting layers are necessary for full-colour devices. Currently, inkjet-printed LEDs have been successfully commercialized, and the infrastructure and facilities for inkjet processed CQD films are ready for mass production by material (Nanosys QD vision, Nanoco and so on), device (Samsung Electronics, TCL, BOE), and manufacturing equipment companies (Kateeva, Epson). Consequently, the feasibility of large inkjet-based CQD-SCs would be very high.

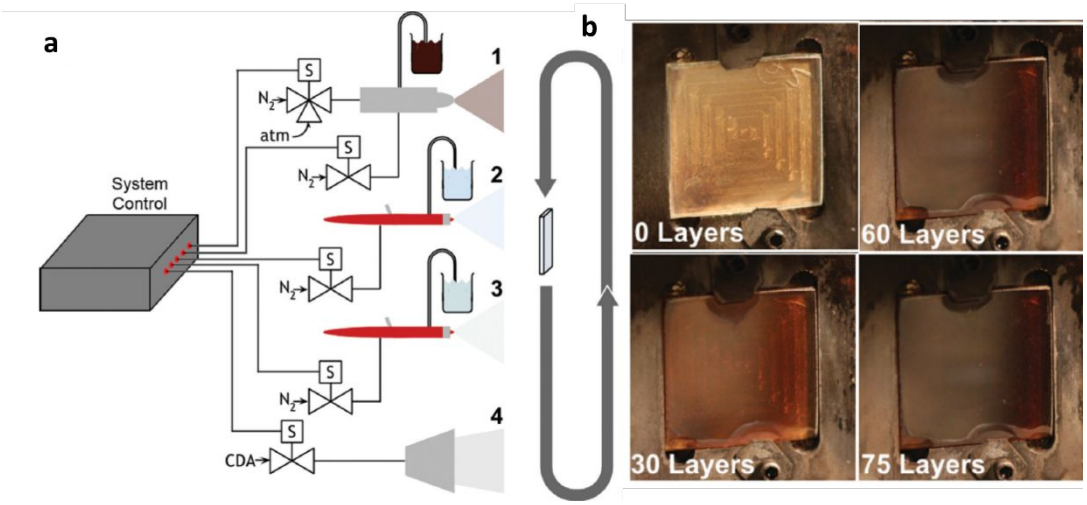

Fig. 16 (a) Schematic of spray coating system for CQD film, (b) Image of CQD films with different number of sprayed layers. Reproduced permission from ref. [40]. Copyright 2015 Wiley.

The spray coating technique is a film deposition method based on the collection of small liquid drops dispersed in a carrier gas. A CQD solution is sprayed through a nozzle using high pressurized gas. All processes can be performed in ambient conditions; thus, an inert-gas-filled glove box is not essential in this approach. Uniformly deposited, large-sized CQD films have been achieved by simply controlling the nozzle and gas pressure. [187, 188] The thickness of CQD film is controllable through a repeatable process, as shown in Fig. 16. Hence, spray coating of CQDs paves the way for forming large-sized, low-cost films. The key issue of the spray coating method is how to uniformly disperse CQDs in the carrier gas and maintain their function. To achieve better film quality, long ligand-capped CQDs are normally dispersed in a solvent. Then, the pressurized inert gas forces CQDs to move and deposit on the substrate. After that, the ligand is exchanged for a short ligand to boost carrier transport among nanocrystals. A comparison of spin- and spray-coated films indicates that the surface of a spray-coated layer is smoother. [40] In addition, pinholes and defects are significantly suppressed in spray-coated films, resulting in an increased minority carrier lifetime and an enhanced diffusion length of CQDs. These benefits have led to a uniform performance of CQD-SCs fabricated by spray coating (PCE of 8.1 ± 0.7%). In addition, the possibility of a roll-to-roll process via spray coating was

also verified with flexible substrate-based SCs.[171]

The last possible upscaling method is doctor-blade or slot-die coating, which is widely accepted in the industry for large-area films with reduced material consumption. Using a large dispenser head and a knife, a uniformly coated layer can be achieved in slot-die and/or doctor-blade coating. [189] The amount of ink can be controlled by modifying the head of the slot-die coater and knife of the doctor-blade coater, which enables the deposition of a film with the desired thickness. Moreover, this process is compatible with a cost-efficient roll-to-roll process. Utilizing these advantages, many research groups have successfully demonstrated slot-die- or doctor-blade-processed SCs with solution-processed light absorbers, including chalcogenide, perovskite and organic materials. [190] CQDs are also soluble materials; thus, attempts to realize large-area films using these techniques have been made. [2] According to Kirmani et al., the introduction of a slot-die-coated film resulted in significantly reduced material consumption (only 4%) compared to the film deposited by the spin coating method. In addition, ambient humidity and oxygen can act as dopants of the CQD ink in slot-die coating, leading to enhanced electrical properties of the films with these dopants, as introduced in Section 2. By employing a high-speed coating process, meeting the industrial requirements (> 15 m/min), a PCE of 10.3% was obtained. A summarized comparison of the different deposition techniques for CQD-SCs is presented in Table 3. As of now, doctor-blade or slot-die coating techniques seem the most promising for mass production. Further intensive studies on enlarging CQD films will result in commercially available devices.

5. Obstacles for CQD-SC commercialization

5.1 Economic viability of CQD-SCs

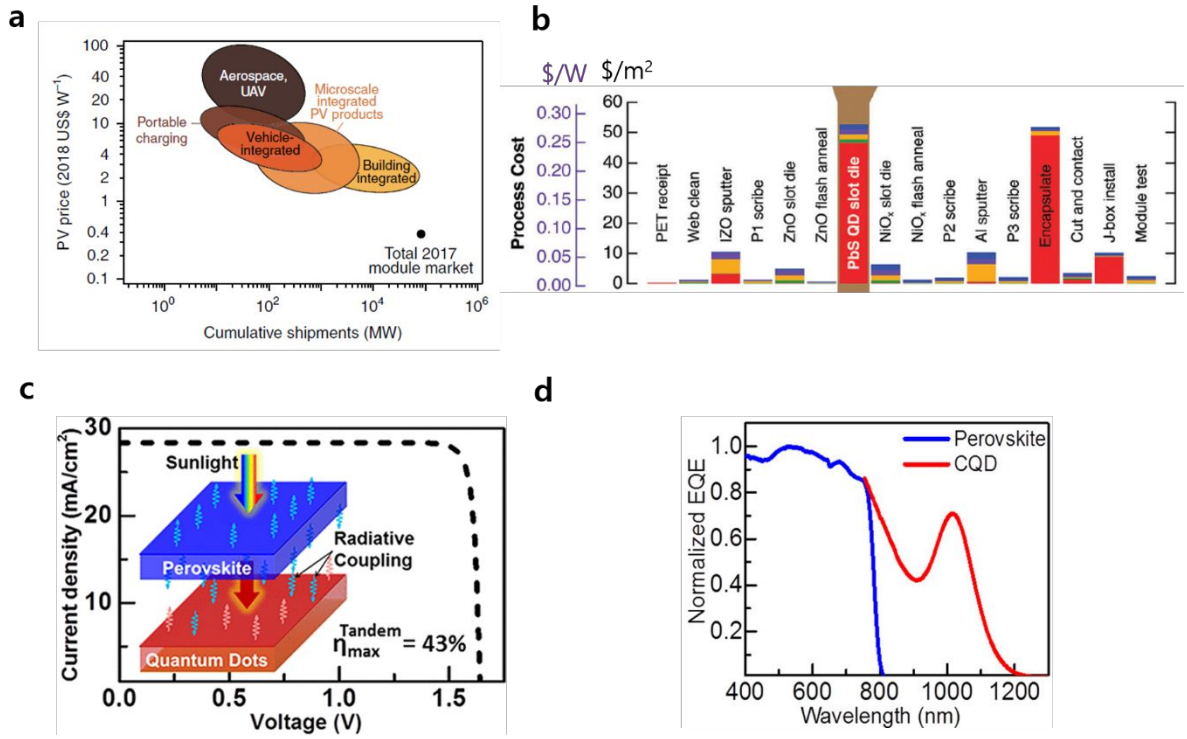

Fig. 17 (a) Projected emerging PV market size as a function of PV price per watt. Reproduced permission from ref. [191]. Copyright 2018, Springer Nature. (b) Manufacturing cost for roll-to-roll processed PV module with flexible substrate (100 um thick PET film). The projected total cost is 0.94 $/W. Here it is assumed that the efficiency of PbS CQD PV module is 19%. Reproduced permission from ref. [192]. Copyright 2018, The Royal Society of Chemistry. (c) c-Si and low band gap CQD tandem cell structure with its theoretically calculated I-V curve and (d) external quantum efficiency under AM 1.5 G condition. Reproduced permission from ref. [193]. Copyright 2018, American Chemical Society.

Commercially available c-Si SCs and their modules are dominant technologies for utility-scale PV power plants. Their market share exceeds 95% owing to their high efficiency (> 20% module efficiency) and low cost (~ 0.2 $/W). Moreover, the output of a c-Si PV module system degrades by less than 20% after 20 years of operation. As a result, the cumulative installation of c-Si SCs is over 500 GW. [194] In addition, more than 2.5% of the world electricity generation is from c-Si PV modules. However, the thick glass sandwich c-Si PV module is too heavy (> 16 kg/m^2), which limits its application (e.g., building- or vehicle-integrated PV modules). Moreover, rigid c-Si PV modules are generally not compatible with portable devices. Although the annual demand of non-utility-type PV modules (portable, aerospace, vehicle-integrated, and microstructure-integrated products) is predicted to be less than 100 MW, only 0.1% of the utility-scale market, this market is growing much faster than the heavy and rigid c-Si PV market. [191] This niche market will be an opportunity for thin-film-based SCs to enter the commercialized market. Compared to the utility-scale PV market, the functionality of solar modules, such as their light weight (W/kg), design, and flexibility, plays very important roles in this area. The projected cost of the emerging flexible PV modules is approximately higher

than 1 $/W, as shown in Fig. 17(a).

Fortunately, CQD-SCs meet the requirements of the niche PV market. Some pioneering works systematically analysed the attainable flexible CQD-SC cost from the viewpoint of elements and processes. Currently, the estimated lowest cost for flexible PbS CQD-SCs is 0.94 $/W, as marked in Fig. 17(b). [192] Here, the efficiency of the CQD-SC (PET film/Induim zinc oxide (IZO)/ZnO/PbS/NiO_X/Al) is assumed to be 19%, and the device is assumed to be manufactured by the roll-to-roll process. According to the survey, the synthesis method using $PbCl_2$ and thioacetamide precursors suggested by Huang et al. significantly decreases labour as well as material costs (0.16 $/W). [195] However, the additional cost of PbS CQD ink preparation for slot-die coating (0.11 $/W) is inevitable in the absorber preparation.[101] Last, common elements for the substrate (0.11 $/W), buffer layer (0.07 $/W), reliable device (encapsulant, 0.27 $/W) and circuit (electrode, contact and junction box, 0.15 $/W) may increase the cost of PbS-CQD PV modules. The common price for roll-to-roll-based SCs still has room for improvement in the high volume market. In addition, the cost of QD ink will be reduced by implementing solvent recycling, developing a robust synthesis method, and automating the process. Further progress in the substrate, encapsulant and CQD ink would accelerate the commercialization of CQD-SCs in the near future.

Another strategy to commercialize CQD-SCs is tandem approaches. As mentioned above, the current cost of a c-Si PV module is approximately 0.2 $/W, which is almost impossible to reach using CQDs as an absorber of SCs considering the current status. [196] Hence, many companies and research institutes, such as Ubiqd, QD Solar Inc, Los Alamos National laboratory, Caltech, and so on tried to find a way to boost performance of c-Si SC with an assist of specially designed QD films and devices. [189, 197-199] Because of the thermodynamic (Shockley-Queisser) limit of light-harvesting materials, the optimized E_g of the active layer for conventional SCs is approximately 1.1 eV. [126, 200] For instance, the E_g values of Si, chalcogenide (CIGS), GaAs, CdTe, and perovskites, which are widely used in conventional SCs, are in the range of 1.1- 1.5 eV. As a result, low energy photons, below E_g (wavelength > 1100 nm), penetrate the cell and do not contribute to the photocurrent in conventional SCs. The total energy of non-absorbed photons is 16.4 mW/cm^2 in conventional single c-Si SCs under the AM 1.5 G solar spectrum.[201, 202] Thus, many research groups have developed small E_g PbS-incorporated SCs and proposed tandem structures consisting of conventional top cells and PbS bottom cells (Please see Fig. 17(c) and (d)). Since lattice matching among light-absorbing films is not necessary in solution-processed devices, a small E_g CQD-SC is versatile for a tandem device. Although the cost of the cell itself increases by implementing a CQD bottom cell, the enhanced performance of the tandem cell with a stack of a conventional device and IR-converting CQDs curtail its levelized cost of electricity.

The energy attainable by introducing a small E_g CQD cell into the tandem structure was theoretically calculated based on experimental results. According to the calculation, the PCE of a tandem cell with a stack of CdTe (E_g=1.5 eV) and IR-absorbing CQD (E_g=0.75 eV) cells reaches over 40%. [90] Moreover, by harnessing solar light in the IR region, a PCE of 29.7% is expected in a monolithic tandem device with perovskite (E_g = 1.55 eV) and PbS CQD (E_g= 1.0 eV) cells. [193] Comparing the certified state-of-the-art perovskite (25.2%) and CQD (16.6%) SCs, more progress is projected in the tandem devices. To realize a highly efficient tandem structure with a conventional device, improvement of the performance of the bottom cell, consisting of small E_g CQDs, is essential. Y. Bi et al. empirically demonstrated a 7.9% efficiency single PbS CQD-SC, whose E_g was below 1.0 eV. [203] In particular, the EQE of the cell was over 80% at 1350 nm. With the assistance of extended photon absorption up to 1400

nm achieved by attaching bottom PbS CQD cells, efficiencies of 3.33 and 0.67% were added to the top perovskite (long pass 750 nm) and c-Si (long pass 1100 nm) SCs, respectively. According to the roadmap of QD solar Inc., more than 4% will be augmented by inserting CQD-SCs at the bottom of c-Si SC systems. [204] Moreover, optimization of the optical structure is projected to lead to better performance of small E_g CQD-SCs located under conventional cells. A selective cavity mirror consisting of multiple layers of an oxide and a nitride reflects IR light, which allows small E_g CQDs to convert more photons to a current. [205] Although further studies are required to improve the stability, interlayer, and optical design, the stack of a conventional solar absorber and low E_g CQDs will successfully provide an opportunity to overcome the Shockley-Queisser limit of a single junction cell.

5.2 Eco-friendly SCs

Table 4. Efficiency of thin-film photovoltaic cells with toxic and non-toxic CQDs

Materials		PCE	Ref
Pb based QD	PbS CQD	12.1%	[18]
	$CSPbI_3$	14.1%	[66]
Non-toxic QD	InZnP	1.2%	[206]
	$AgBiS_2$	6.3%	[207]
	$CuInS_2$	1.2%	[208]

To date, highly efficient devices based on Pb-containing CQDs, such as PbS (PCE of 12.1%) and $CsPbI_3$ (14.1%) nanocrystals, have been reported. However, the use of toxic elements, including Pb, Hg, Cd, and so on, is severely restricted in nearly all commercial electronic devices. Many regulations on the amount of Pb have been imposed. [209] Moreover, end-of-life issues need to be addressed for PV modules containing Pb-based CQDs. Although the Pb based active layer is very thin (hundreds of nanometres), the accumulated Pb from MW- and/or GW-sized CQD PV systems will be non-negligible. C-Si PV modules, which currently dominate the PV market, also face similar problems. Due to environmental regulations, replacement of Pb-containing solders (SnPb) with eco-friendly solders and collection of these solders from aged modules have been intensively studied. [210] As a Cd-containing CQD has been successfully substituted for heavy-metal-free (InP, CIGS, and so on) ones in the commercialized CQD display business, the development of highly efficient CQD-SCs with non-toxic materials is expected. [211-213] Unfortunately, the performance of CQD-SCs with eco-friendly elements is currently inferior to that of PVs with PbS CQDs, as summarized in Table 4. However, progress in new materials and device structure would enable efficient utilization of CQD devices with heavy-metal-free elements.

Among the many possible non-toxic materials, In-based binary and ternary (InAS, InSb, InZnP) QDs have been investigated, which can convert a broad range of solar light (from UV to NIR) into electricity. In-based nanocrystals and their films exhibit excellent optical and electrical properties for optoelectronic devices. Their absorption coefficients are very high such that an only 100 nm film is sufficiently thick to absorb incident photons. [214, 215] Moreover, the electron mobility of films with InAS CQDs exceeds 15 cm^2/Vs in field effect transistor. [216] In addition, the attainable advantage of In-based eco-friendly CQDs is the enhanced MEG, because their CM threshold is near $2E_g$. [217] Moreover, In based QD shows excellent stability under high voltage field, reported by Samsung Electronics. [218] Despite the excellent optical and electrical

properties of In-based CQDs, the reported efficiencies of solid-state SCs with 3.2 nm InP and 2.8 nm InZnP CQDs were only 0.7 and 1.2%, respectively. [206] This result was mainly attributed to the poly-dispersity of the CQD size and increased recombination losses induced by poor CQD surface passivation. [219, 220] For the better performance of In based CQD SCs, these issues should be overcame. Meanwhile, implementation of In-based CQDs in SCs as a buffer layer rather than an active layer was suggested. As the In-based nanocrystal layer exhibits very high mobility, the incorporation of In-based CQD film into a SC led to improved carrier collection efficiency. Moreover, the E_g of the In-based QD can be tuned by surface treatment, enabling the desired band alignment between the electrode and active layer. Song et al. inserted an InAs QD layer between an electrode and a p-n-type PbS QD active layer. [221] The air-stable InAs QD film boosted the carrier collection efficiency, thereby leading to improved *FF* (0.39 ➔ 0.63), J_{SC} (13.13 ➔ 20.92 mA/cm^2), V_{OC} (0.21 ➔ 0.54 V), and PCE (1.1 ➔ 7.2%). Although the active layer still consisted of Pb-based CQDs, this work revealed that surface-treated InAs QDs have potential to realize eco-benign CQD-SCs.

Another possible candidate for non-toxic CQD-SCs is Ag- and Sb-based compound nanocrystals (Sb_2Se_3, Ag_2S, $AgBiS_2$, $AgBiSe_3$). The bulk E_g of these materials are narrow, so they can absorb a wide range of IR light (i.e., bulk E_g of $AgBiS_2$: 1.1 eV, Ag_2S: 1.07 eV, Ag_2Se: 0.17 eV, Sb_2Se_3: 1.0 eV). [207, 222, 223] As a result, intensive studies to develop SCs using their bulk materials have been conducted. Solid thin-film SCs with a bulk Sb_2Se_3 layer showed promising efficiency (PCE of 7.5-9.2%).[224, 225] This result was achieved without high cost (In and Ga) or toxic (Cd and Pb) materials. However, the excellent properties of bulk Sb_2Se_3 have not been linked to a highly efficient CQD-SC because of its poor size control and corrosion during the synthesis process. [223] Regardless of the many obstacles for realizing highly efficient non-toxic CQD-SCs, such as the poor understanding of the CQD surface passivation, charge transport inside the film, and CQD composition, a record high PCE of 6.31% has been achieved using $AgBiS_2$ QDs. [207] The E_g of $AgBiS_2$ lies between those of ZnO and the p-type polymer layer; thus, the introduction of an ETL and an HTL boosts the photogenerated carrier collection efficiency in $AgBiS_2$ CQD-SCs. Further modification of the surface passivation and size control of Ag- and Sb-based CQDs is predicted to help overcome the limitations of their devices by minimizing recombination losses and maximizing light absorption.

Last, CQDs consisting of chalcopyrite (e.g., $CnInGaSe_2$) have also been considered non-toxic alternatives. For the bulk film, the record efficiency of a Cu-In-Ga-Se SC exceeded 20%, and this cell is competitive with other thin-film and c-Si PV cells in the commercialized market. [226] Because of the strong absorption coefficient and the possibility of tuning the E_g, chalcopyrite CQD optoelectronic devices have been intensively studied. [227] However, the studies mainly focused on dye-sensitized SCs rather than on solid-type SCs owing to inefficient charge transport in the CQD film. The delocalized ions and Cu vacancies in chalcopyrite CQDs contribute to broadening of the CB and VB, which act as trap sites in the solid film. [228, 229] In particular, the intra-gap state dramatically decreases the carrier mobility. As a result, a PCE of only 1.1% was obtained in solid-type chalcopyrite CQD-SCs, while the certified PCE of dye-sensitized-type chalcopyrite CQDs was 11.6%. [208, 227] Since thermal annealing of films and control of elements may reduce the defect states of chalcopyrite CQDs, control of the carrier transport inside the chalcopyrite CQD film is necessary for developing solid-type SCs with it.

6. Conclusion and remarks

CQD-SCs have been considered a strong candidate for next-generation energy sources. By utilizing the quantum confinement effect, efficient colour-tuneable SCs with varying CQD sizes can be fabricated. Along with the improvement of CQD materials and surface chemistry for the last decade, many studies have focused on improving the PV performance of the devices. The development of device engineering has led to an enlarging depletion region and efficient charge extraction of photogenerated charges, achieving an over 16% certified PCE. CQDs exhibit several advantageous features compared to competing emerging PV materials: (1) control of E_g by tuning the CQD size, (2) energy level alignment via surface treatment, (3) low MEG threshold, (4) utilization of infrared light, and (5) possible use of air-stable inorganic materials for all device layers. Moreover, CQDs exhibit high feasibility for film deposition through solution processes. Industrial film deposition methods, such as inkjet printing, doctor blading and slot-die coating, can be used in CQD film deposition. Furthermore, post-treatment (high-temperature annealing) would not be required for CQD film deposition. The most competitive emerging PVs, perovskites, require very fine film quality to achieve a high PCE. The anti-solvent dripping process (which is essential for the fine film quality) during the spin coating of perovskite solution is a large bottleneck for the upscaling process. Another possible candidate for competitive emerging PVs is organic photovoltaics (OPVs). The reported high-efficiency OPVs have a very high cost for synthesizing the polymers. Thus, CQD-SCs are one of the most promising candidates for next-generation PVs. CQD-SC are expected to enter the flexible, portable PV market in the near future. Moreover, stacks of conventional (c-Si or thin-film) SCs and low E_g CQD-SCs can overcome the efficiency limit of a single cell. However, some issues should be addressed for the successful commercialization of CQD-SCs.

The most urgent issues to be handled are the device stability and environmental toxicity of the materials. The operational lifetime of the devices under illumination is only 1100 hours at the T_{80} point. If proper device encapsulation excludes other environmental degradation sources, such as oxygen and humidity, then the remaining unsolved issue will be improving the stability of the light-unstable parts in CQD devices. The hydroxide parts on the CQD surfaces should be effectively passivated by ligand exchange or surface treatments. Replacement or passivation (doping) with light-stable materials of the most widely used light-unstable ETL, ZnO, is required. To date, metal doping of ZnO has exhibited the most effective defect passivation characteristics, but not enough to satisfy commercial standards. Additionally, the interfacial junctions from each PV constituent layer should be carefully investigated. The defect states at these junctions could act as non-radiative recombination centres during operation under illumination.

The highest-performing CQD-SCs consist of Pb-included elements, which are strictly regulated for commercial usage. Although the total amount of Pb for a single device is almost negligible, the amount would be considerable when the single devices are integrated into PV modules. Less toxic candidate materials, such as In, As, or Sb, have been investigated to achieve eco-friendly and efficient CQD-SCs. However, difficulties in CQD size control or in the synthesis process need to be overcome in these materials. Although non-Pb-based CQD-SCs have shown a maximum PCE of only ~6%, they have been reported to exhibit promising characteristics, such as high mobility and absorption coefficient. Thus, further investigation of these materials to realize eco-friendly and efficient CQD-SCs would be very promising.

Once the outstanding advantages of CQDs can be effectively utilized in device physics and materials science, commercialization of CQD-SCs will no longer be uncertain, and CQD-SCs will take a portion of the future PV markets.

Acknowledgements

This work is supported by the National Science Foundation (NSF, grant no. 1808163). Hyung-Jun Song acknowledges the New & Renewable Energy Technology Development Program of the Korea Institute of Energy Technology Evaluation and Planning (KETEP) grant, funded by the Ministry of Trade, Industry and Energy, Korea (No. 20193010014570) and National Research Foundation of Korea (NRF) through the Basic Science Research Program (NRF-2019R1F1A1057693).

Table of Contents

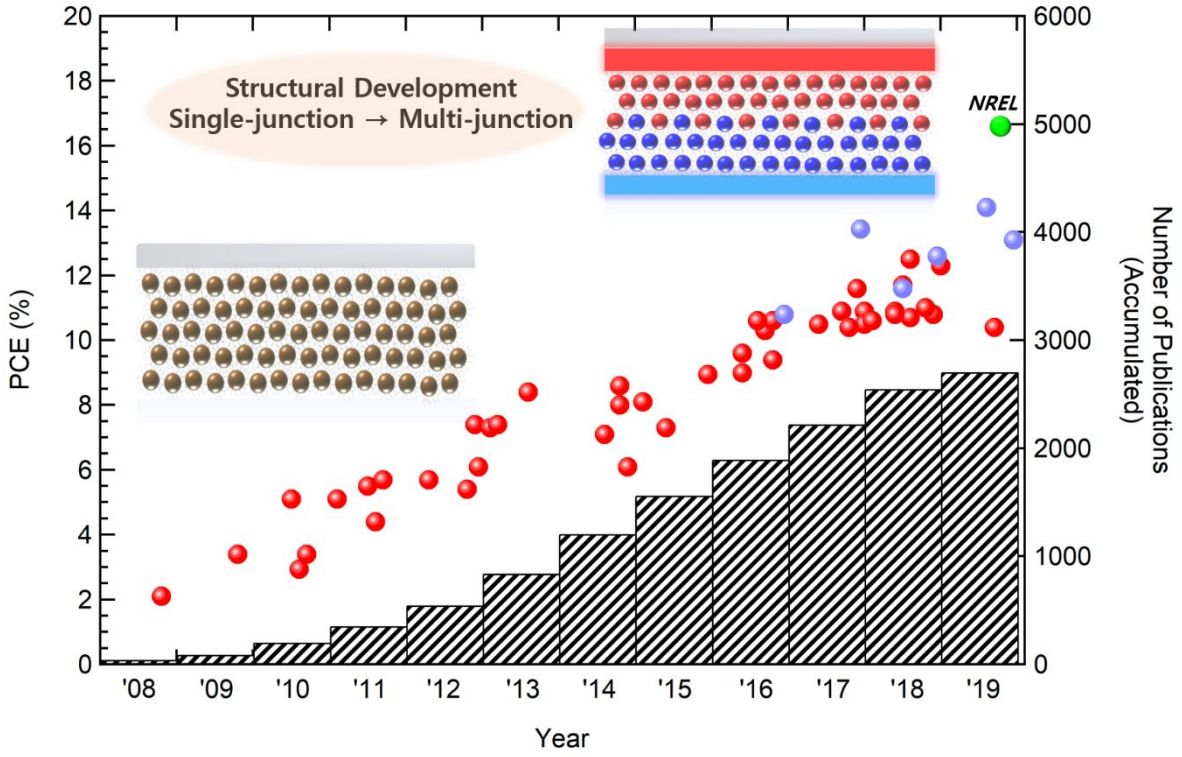

A review towards commercialization of colloidal quantum dot solar cells.

References

1. A. Kongkanand, K. Tvrdy, K. Takechi, M. Kuno and P. V. Kamat, *J. Am. Chem. Soc.*, 2008, **130**, 4007-4015.
2. A. R. Kirmani, A. D. Sheikh, M. R. Niazi, M. A. Haque, M. Liu, F. P. G. de Arquer, J. Xu, B. Sun, O. Voznyy, N. Gasparini, D. Baran, T. Wu, E. H. Sargent and A. Amassian, *Adv. Mater.*, 2018, **30**, 1801661.
3. C. R. Kagan, E. Lifshitz, E. H. Sargent and D. V. Talapin, *Science*, 2016, **353**, aac5523.
4. H. J. Jang, J. Y. Lee, J. Kwak, D. Lee, J.-H. Park, B. Lee and Y. Y. Noh, *J. Inf. Disp.*, 2019, **20**,

1-8.

5. Z. Hens and I. Moreels, *J. Mater. Chem.*, 2012, **22**, 10406-10415.
6. J.-S. Lee, M. V. Kovalenko, J. Huang, D. S. Chung and D. V. Talapin, *Nat. Nanotechnol.*, 2011, **6**, 348.
7. J.-H. Choi, A. T. Fafarman, S. J. Oh, D.-K. Ko, D. K. Kim, B. T. Diroll, S. Muramoto, J. G. Gillen, C. B. Murray and C. R. Kagan, *Nano Lett.*, 2012, **12**, 2631-2638.
8. M. Nam, S. Kim, S. Kim, S.-W. Kim and K. Lee, *Nanoscale*, 2013, **5**, 8202-8209.
9. H. Lee, J. Lim, J. Song, H. Heo, K. An, J. Kim, S. Lee, K. Char, H.-J. Song and C. Lee, *Nanotechnology*, 2018, **30**, 065401.
10. S. Lee, J. C. Flanagan, J. Kim, A. J. Yun, B. Lee, M. Shim and B. Park, *ACS Appl. Mater. Interfaces*, 2019, **11**, 19104-19114.
11. S. J. Oh, Z. Wang, N. E. Berry, J.-H. Choi, T. Zhao, E. A. Gaulding, T. Paik, Y. Lai, C. B. Murray and C. R. Kagan, *Nano Lett.*, 2014, **14**, 6210-6216.
12. M. J. Speirs, D. N. Dirin, M. Abdu-Aguye, D. M. Balazs, M. V. Kovalenko and M. A. Loi, *Energy Environ. Sci.,* 2016, **9**, 2916-2924.
13. V. I. Klimov, *Annu. Rev. Condens. Matter Phys.,* 2014, **5**, 285-316.
14. O. E. Semonin, J. M. Luther, S. Choi, H.-Y. Chen, J. Gao, A. J. Nozik and M. C. Beard, *Science*, 2011, **334**, 1530-1533.
15. A. Rao and R. H. Friend, *Nat. Rev. Mater.*, 2017, **2**, 17063.
16. D. Hahm, D. Ko, B. G. Jeong, S. Jeong, J. Lim, W. K. Bae, C. Lee and K. Char, *J. Inf. Disp.*, 2019, **20**, 61-72.
17. *https://www.pv-tech.org/news/hanergys-new-business-model-is-selling-thin-film-production-lines-to-indust*.
18. NREL, Solar Cell Efficiency Chart. Available online: https://www.nrel.gov/pv/assets/pdfs/best-research-cell-efficiencies.20191210.pdf (accessed on 10 December 2019)).
19. J. M. Luther, M. Law, M. C. Beard, Q. Song, M. O. Reese, R. J. Ellingson and A. J. Nozik, *Nano Lett.*, 2008, **8**, 3488-3492.
20. J. J. Choi, Y.-F. Lim, M. E. B. Santiago-Berrios, M. Oh, B.-R. Hyun, L. Sun, A. C. Bartnik, A. Goedhart, G. G. Malliaras, H. D. Abruña, F. W. Wise and T. Hanrath, *Nano Lett.*, 2009, **9**, 3749-3755.
21. J. M. Luther, J. Gao, M. T. Lloyd, O. E. Semonin, M. C. Beard and A. J. Nozik, *Adv. Mater.*, 2010, **22**, 3704-3707.
22. R. Debnath, M. T. Greiner, I. J. Kramer, A. Fischer, J. Tang, D. A. R. Barkhouse, X. Wang, L. Levina, Z.-H. Lu and E. H. Sargent, *Appl. Phys. Lett.*, 2010, **97**, 023109.
23. A. G. Pattantyus-Abraham, I. J. Kramer, A. R. Barkhouse, X. Wang, G. Konstantatos, R. Debnath, L. Levina, I. Raabe, M. K. Nazeeruddin, M. Grätzel and E. H. Sargent, *ACS Nano*, 2010, **4**, 3374-3380.
24. D. A. R. Barkhouse, R. Debnath, I. J. Kramer, D. Zhitomirsky, A. G. Pattantyus-Abraham, L. Levina, L. Etgar, M. Grätzel and E. H. Sargent, *Adv. Mater.*, 2011, **23**, 3134-3138.

25. J. Gao, C. L. Perkins, J. M. Luther, M. C. Hanna, H.-Y. Chen, O. E. Semonin, A. J. Nozik, R. J. Ellingson and M. C. Beard, *Nano Lett.*, 2011, **11**, 3263-3266.
26. H. Liu, J. Tang, I. J. Kramer, R. Debnath, G. I. Koleilat, X. Wang, A. Fisher, R. Li, L. Brzozowski, L. Levina and E. H. Sargent, *Adv. Mater.*, 2011, **23**, 3832-3837.
27. J. Tang, K. W. Kemp, S. Hoogland, K. S. Jeong, H. Liu, L. Levina, M. Furukawa, X. Wang, R. Debnath, D. Cha, K. W. Chou, A. Fischer, A. Amassian, J. B. Asbury and E. H. Sargent, *Nat. Mater.*, 2011, **10**, 765.
28. A. H. Ip, S. M. Thon, S. Hoogland, O. Voznyy, D. Zhitomirsky, R. Debnath, L. Levina, L. R. Rollny, G. H. Carey, A. Fischer, K. W. Kemp, I. J. Kramer, Z. Ning, A. J. Labelle, K. W. Chou, A. Amassian and E. H. Sargent, *Nat. Nanotechnol.*, 2012, **7**, 577.
29. I. J. Kramer, D. Zhitomirsky, J. D. Bass, P. M. Rice, T. Topuria, L. Krupp, S. M. Thon, A. H. Ip, R. Debnath, H.-C. Kim and E. H. Sargent, *Adv. Mater.*, 2012, **24**, 2315-2319.
30. H. Liu, D. Zhitomirsky, S. Hoogland, J. Tang, I. J. Kramer, Z. Ning and E. H. Sargent, *Appl. Phys. Lett.*, 2012, **101**, 151112.
31. J. Tang, H. Liu, D. Zhitomirsky, S. Hoogland, X. Wang, M. Furukawa, L. Levina and E. H. Sargent, *Nano Lett.*, 2012, **12**, 4889-4894.
32. X. Lan, J. Bai, S. Masala, S. M. Thon, Y. Ren, I. J. Kramer, S. Hoogland, A. Simchi, G. I. Koleilat, D. Paz-Soldan, Z. Ning, A. J. Labelle, J. Y. Kim, G. Jabbour and E. H. Sargent, *Adv. Mater.*, 2013, **25**, 1769-1773.
33. P. Maraghechi, A. J. Labelle, A. R. Kirmani, X. Lan, M. M. Adachi, S. M. Thon, S. Hoogland, A. Lee, Z. Ning, A. Fischer, A. Amassian and E. H. Sargent, *ACS Nano*, 2013, **7**, 6111-6116.
34. Z. Ning, D. Zhitomirsky, V. Adinolfi, B. Sutherland, J. Xu, O. Voznyy, P. Maraghechi, X. Lan, S. Hoogland, Y. Ren and E. H. Sargent, *Adv. Mater.*, 2013, **25**, 1719-1723.
35. C.-H. M. Chuang, P. R. Brown, V. Bulović and M. G. Bawendi, *Nat. Mater.*, 2014, **13**, 796.
36. A. R. Kirmani, G. H. Carey, M. Abdelsamie, B. Yan, D. Cha, L. R. Rollny, X. Cui, E. H. Sargent and A. Amassian, *Adv. Mater.*, 2014, **26**, 4717-4723.
37. Z. Ning, H. Dong, Q. Zhang, O. Voznyy and E. H. Sargent, *ACS Nano*, 2014, **8**, 10321-10327.
38. Z. Ning, O. Voznyy, J. Pan, S. Hoogland, V. Adinolfi, J. Xu, M. Li, A. R. Kirmani, J.-P. Sun, J. Minor, K. W. Kemp, H. Dong, L. Rollny, A. Labelle, G. Carey, B. Sutherland, I. Hill, A. Amassian, H. Liu, J. Tang, O. M. Bakr and E. H. Sargent, *Nat. Mater.*, 2014, **13**, 822.
39. R. W. Crisp, D. M. Kroupa, A. R. Marshall, E. M. Miller, J. Zhang, M. C. Beard and J. M. Luther, *Sci. Rep.*, 2015, **5**, 9945.
40. I. J. Kramer, J. C. Minor, G. Moreno-Bautista, L. Rollny, P. Kanjanaboos, D. Kopilovic, S. M. Thon, G. H. Carey, K. W. Chou, D. Zhitomirsky, A. Amassian and E. H. Sargent, *Adv. Mater.*, 2015, **27**, 116-121.
41. Z. Yang, A. Janmohamed, X. Lan, F. P. García de Arquer, O. Voznyy, E. Yassitepe, G.-H. Kim, Z. Ning, X. Gong, R. Comin and E. H. Sargent, *Nano Lett.*, 2015, **15**, 7539-7543.
42. R. Azmi, H. Aqoma, W. T. Hadmojo, J.-M. Yun, S. Yoon, K. Kim, Y. R. Do, S.-H. Oh and S.-Y. Jang, *Adv. Energy Mater.*, 2016, **6**, 1502146.

43. R. Azmi, S.-H. Oh and S.-Y. Jang, *ACS Energy Lett.*, 2016, **1**, 100-106.
44. Y. Cao, A. Stavrinadis, T. Lasanta, D. So and G. Konstantatos, *Nat. Energy*, 2016, **1**, 16035.
45. Z. Jin, M. Yuan, H. Li, H. Yang, Q. Zhou, H. Liu, X. Lan, M. Liu, J. Wang, E. H. Sargent and Y. Li, *Adv. Funct. Mater.*, 2016, **26**, 5284-5289.
46. X. Lan, O. Voznyy, F. P. García de Arquer, M. Liu, J. Xu, A. H. Proppe, G. Walters, F. Fan, H. Tan, M. Liu, Z. Yang, S. Hoogland and E. H. Sargent, *Nano Lett.*, 2016, **16**, 4630-4634.
47. A. Swarnkar, A. R. Marshall, E. M. Sanehira, B. D. Chernomordik, D. T. Moore, J. A. Christians, T. Chakrabarti and J. M. Luther, *Science*, 2016, **354**, 92-95.
48. R. Azmi, S. Y. Nam, S. Sinaga, S.-H. Oh, T. K. Ahn, S. C. Yoon, I. H. Jung and S.-Y. Jang, *Nano Energy*, 2017, **39**, 355-362.
49. J. Choi, Y. Kim, J. W. Jo, J. Kim, B. Sun, G. Walters, F. P. García de Arquer, R. Quintero-Bermudez, Y. Li, C. S. Tan, L. N. Quan, A. P. T. Kam, S. Hoogland, Z. Lu, O. Voznyy and E. H. Sargent, *Adv. Mater.*, 2017, **29**, 1702350.
50. J. W. Jo, Y. Kim, J. Choi, F. P. G. de Arquer, G. Walters, B. Sun, O. Ouellette, J. Kim, A. H. Proppe, R. Quintero-Bermudez, J. Fan, J. Xu, C. S. Tan, O. Voznyy and E. H. Sargent, *Adv. Mater.*, 2017, **29**, 1703627.
51. A. Stavrinadis, S. Pradhan, P. Papagiorgis, G. Itskos and G. Konstantatos, *ACS Energy Lett.*, 2017, **2**, 739-744.
52. Z. Yang, J. Z. Fan, A. H. Proppe, F. P. G. d. Arquer, D. Rossouw, O. Voznyy, X. Lan, M. Liu, G. Walters, R. Quintero-Bermudez, B. Sun, S. Hoogland, G. A. Botton, S. O. Kelley and E. H. Sargent, *Nat. Commun.*, 2017, **8**, 1325.
53. X. Zhang, P. K. Santra, L. Tian, M. B. Johansson, H. Rensmo and E. M. J. Johansson, *ACS Nano*, 2017, **11**, 8478-8487.
54. E. M. Sanehira, A. R. Marshall, J. A. Christians, S. P. Harvey, P. N. Ciesielski, L. M. Wheeler, P. Schulz, L. Y. Lin, M. C. Beard and J. M. Luther, *Sci. Adv.*, 2017, **3**, eaao4204.
55. H. Aqoma and S.-Y. Jang, *Energy Environ. Sci.*, 2018, **11**, 1603-1609.
56. R. Azmi, G. Seo, T. K. Ahn and S.-Y. Jang, *ACS Appl. Mater. Interfaces*, 2018, **10**, 35244-35249.
57. S.-W. Baek, S.-H. Lee, J. H. Song, C. Kim, Y.-S. Ha, H. Shin, H. Kim, S. Jeong and J.-Y. Lee, *Energy Environ. Sci.*, 2018, **11**, 2078-2084.
58. L. Hu, Z. Zhang, R. J. Patterson, Y. Hu, W. Chen, C. Chen, D. Li, C. Hu, C. Ge, Z. Chen, L. Yuan, C. Yan, N. Song, Z. L. Teh, G. J. Conibeer, J. Tang and S. Huang, *Nano Energy*, 2018, **46**, 212-219.
59. J. Kim, O. Ouellette, O. Voznyy, M. Wei, J. Choi, M.-J. Choi, J. W. Jo, S.-W. Baek, J. Fan, M. I. Saidaminov, B. Sun, P. Li, D.-H. Nam, S. Hoogland, Z.-H. Lu, F. P. García de Arquer and E. H. Sargent, *Adv. Mater.*, 2018, **30**, 1803830.
60. K. Lu, Y. Wang, Z. Liu, L. Han, G. Shi, H. Fang, J. Chen, X. Ye, S. Chen, F. Yang, A. G. Shulga, T. Wu, M. Gu, S. Zhou, J. Fan, M. A. Loi and W. Ma, *Adv. Mater.*, 2018, **30**, 1707572.
61. Y. Wang, K. Lu, L. Han, Z. Liu, G. Shi, H. Fang, S. Chen, T. Wu, F. Yang, M. Gu, S. Zhou, X.

Ling, X. Tang, J. Zheng, M. A. Loi and W. Ma, *Adv. Mater.*, 2018, **30**, 1704871.

62. J. Xu, O. Voznyy, M. Liu, A. R. Kirmani, G. Walters, R. Munir, M. Abdelsamie, A. H. Proppe, A. Sarkar, F. P. García de Arquer, M. Wei, B. Sun, M. Liu, O. Ouellette, R. Quintero-Bermudez, J. Li, J. Fan, L. Quan, P. Todorovic, H. Tan, S. Hoogland, S. O. Kelley, M. Stefik, A. Amassian and E. H. Sargent, *Nat. Nanotechnol.*, 2018, **13**, 456-462.
63. Q. Wang, Z. Jin, D. Chen, D. Bai, H. Bian, J. Sun, G. Zhu, G. Wang and S. Liu, *Adv. Energy Mater.*, 2018, **8**, 1800007.
64. J. Yuan, X. Ling, D. Yang, F. Li, S. Zhou, J. Shi, Y. Qian, J. Hu, Y. Sun, Y. Yang, X. Gao, S. Duhm, Q. Zhang and W. Ma, *Joule*, 2018, **2**, 2450-2463.
65. L. Hu, X. Geng, S. Singh, J. Shi, Y. Hu, S. Li, X. Guan, T. He, X. Li, Z. Cheng, R. Patterson, S. Huang and T. Wu, *Nano Energy*, 2019, **64**, 103922.
66. X. Ling, S. Zhou, J. Yuan, J. Shi, Y. Qian, B. W. Larson, Q. Zhao, C. Qin, F. Li, G. Shi, C. Stewart, J. Hu, X. Zhang, J. M. Luther, S. Duhm and W. Ma, *Adv. Energy Mater.*, 2019, **9**, 1900721.
67. J. Shi, F. Li, J. Yuan, X. Ling, S. Zhou, Y. Qian and W. Ma, *J. Mater. Chem. A*, 2019, **7**, 20936-20944.
68. J. P. Clifford, K. W. Johnston, L. Levina and E. H. Sargent, *Appl. Phys. Lett.*, 2007, **91**, 253117.
69. C. Piliego, L. Protesescu, S. Z. Bisri, M. V. Kovalenko and M. A. Loi, *Energy Environ. Sci.*, 2013, **6**, 3054-3059.
70. M.-J. Choi, J. Oh, J.-K. Yoo, J. Choi, D. M. Sim and Y. S. Jung, *Energy Environ. Sci.*, 2014, **7**, 3052-3060.
71. J. Tang, X. Wang, L. Brzozowski, D. A. R. Barkhouse, R. Debnath, L. Levina and E. H. Sargent, *Adv. Mater.*, 2010, **22**, 1398-1402.
72. X.-D. Mai, H. J. An, J. H. Song, J. Jang, S. Kim and S. Jeong, *J. Mater. Chem. A*, 2014, **2**, 20799-20805.
73. M.-J. Choi, S. Kim, H. Lim, J. Choi, D. M. Sim, S. Yim, B. T. Ahn, J. Y. Kim and Y. S. Jung, *Adv. Mater.*, 2016, **28**, 1780-1787.
74. H. Lee, H. C. Leventis, S.-J. Moon, P. Chen, S. Ito, S. A. Haque, T. Torres, F. Nüesch, T. Geiger, S. M. Zakeeruddin, M. Grätzel and M. K. Nazeeruddin, *Adv. Funct. Mater.*, 2009, **19**, 2735-2742.
75. N. Zhao, T. P. Osedach, L.-Y. Chang, S. M. Geyer, D. Wanger, M. T. Binda, A. C. Arango, M. G. Bawendi and V. Bulovic, *ACS Nano*, 2010, **4**, 3743-3752.
76. S. M. Willis, C. Cheng, H. E. Assender and A. A. R. Watt, *Nano Lett.*, 2012, **12**, 1522-1526.
77. J. Jean, S. Chang, P. R. Brown, J. J. Cheng, P. H. Rekemeyer, M. G. Bawendi, S. Gradečak and V. Bulović, *Adv. Mater.*, 2013, **25**, 2790-2796.
78. S.-W. Baek, P. Molet, M.-J. Choi, M. Biondi, O. Ouellette, J. Fan, S. Hoogland, F. P. García de Arquer, A. Mihi and E. H. Sargent, *Adv. Mater.*, **0**, 1901745.
79. A. K. Rath, M. Bernechea, L. Martinez, F. P. G. de Arquer, J. Osmond and G. Konstantatos, *Nat. Photonics*, 2012, **6**, 529.
80. A. Stavrinadis, A. K. Rath, F. P. G. de Arquer, S. L. Diedenhofen, C. Magén, L. Martinez, D. So

and G. Konstantatos, *Nat. Commun.*, 2013, **4**, 2981.

81. T. Zhao, E. D. Goodwin, J. Guo, H. Wang, B. T. Diroll, C. B. Murray and C. R. Kagan, *ACS Nano*, 2016, **10**, 9267-9273.
82. M. Yuan, D. Zhitomirsky, V. Adinolfi, O. Voznyy, K. W. Kemp, Z. Ning, X. Lan, J. Xu, J. Y. Kim, H. Dong and E. H. Sargent, *Adv. Mater.*, 2013, **25**, 5586-5592.
83. R. Wang, X. Wu, K. Xu, W. Zhou, Y. Shang, H. Tang, H. Chen and Z. Ning, *Adv. Mater.*, 2018, **30**, 1704882.
84. J. J. Choi, W. N. Wenger, R. S. Hoffman, Y.-F. Lim, J. Luria, J. Jasieniak, J. A. Marohn and T. Hanrath, *Adv. Mater.*, 2011, **23**, 3144-3148.
85. X. Wang, G. I. Koleilat, J. Tang, H. Liu, I. J. Kramer, R. Debnath, L. Brzozowski, D. A. R. Barkhouse, L. Levina, S. Hoogland and E. H. Sargent, *Nat. Photonics*, 2011, **5**, 480.
86. M. J. Speirs, B. G. H. M. Groeneveld, L. Protesescu, C. Piliego, M. V. Kovalenko and M. A. Loi, *Phys. Chem. Chem. Phys.*, 2014, **16**, 7672-7676.
87. T. Kim, Y. Gao, H. Hu, B. Yan, Z. Ning, L. K. Jagadamma, K. Zhao, A. R. Kirmani, J. Eid, M. M. Adachi, E. H. Sargent, P. M. Beaujuge and A. Amassian, *Nano Energy*, 2015, **17**, 196-205.
88. T. Kim, Y. Firdaus, A. R. Kirmani, R.-Z. Liang, H. Hu, M. Liu, A. El Labban, S. Hoogland, P. M. Beaujuge, E. H. Sargent and A. Amassian, *ACS Energy Lett.*, 2018, **3**, 1307-1314.
89. Y. Zhang, M. Gu, N. Li, Y. Xu, X. Ling, Y. Wang, S. Zhou, F. Li, F. Yang, K. Ji, J. Yuan and W. Ma, *J. Mater. Chem. A*, 2018, **6**, 24693-24701.
90. R. W. Crisp, G. F. Pach, J. M. Kurley, R. M. France, M. O. Reese, S. U. Nanayakkara, B. A. MacLeod, D. V. Talapin, M. C. Beard and J. M. Luther, *Nano Lett.*, 2017, **17**, 1020-1027.
91. G. Shi, Y. Wang, Z. Liu, L. Han, J. Liu, Y. Wang, K. Lu, S. Chen, X. Ling, Y. Li, S. Cheng and W. Ma, *Adv. Energy Mater.*, 2017, **7**, 1602667.
92. Y. Bi, S. Pradhan, M. Z. Akgul, S. Gupta, A. Stavrinadis, J. Wang and G. Konstantatos, *ACS Energy Lett.*, 2018, **3**, 1753-1759.
93. Y. Gao, J. Zheng, W. Chen, L. Yuan, Z. L. Teh, J. Yang, X. Cui, G. Conibeer, R. Patterson and S. Huang, *J. Phys. Chem. Lett.*, 2019, **10**, 5729-5734.
94. J. Kim, B. G. Jeong, H. Roh, J. Song, M. Park, D. C. Lee, W. K. Bae and C. Lee, *ACS Applied Materials & Interfaces*, 2016, **8**, 23947-23952.
95. D. Mandal and A. K. Rath, *ACS Appl. Mater. Interfaces*, 2018, **10**, 39074-39082.
96. Q. A. Akkerman, M. Gandini, F. Di Stasio, P. Rastogi, F. Palazon, G. Bertoni, J. M. Ball, M. Prato, A. Petrozza and L. Manna, *Nat. Energy*, 2016, **2**, 16194.
97. F. Li, S. Zhou, J. Yuan, C. Qin, Y. Yang, J. Shi, X. Ling, Y. Li and W. Ma, *ACS Energy Lett.*, 2019, **4**, 2571-2578.
98. Q. Zhao, A. Hazarika, X. Chen, S. P. Harvey, B. W. Larson, G. R. Teeter, J. Liu, T. Song, C. Xiao, L. Shaw, M. Zhang, G. Li, M. C. Beard and J. M. Luther, *Nat. Commun.*, 2019, **10**, 2842.
99. R. Wang, Y. Shang, P. Kanjanaboos, W. Zhou, Z. Ning and E. H. Sargent, *Energy Environ. Sci.*, 2016, **9**, 1130-1143.
100. O. Voznyy, D. Zhitomirsky, P. Stadler, Z. Ning, S. Hoogland and E. H. Sargent, *ACS Nano*,

2012, **6**, 8448-8455.

101. M. Liu, O. Voznyy, R. Sabatini, F. P. García de Arquer, R. Munir, Ahmed H. Balawi, X. Lan, F. Fan, G. Walters, Ahmad R. Kirmani, S. Hoogland, F. Laquai, A. Amassian and Edward H. Sargent, *Nat. Mater.*, 2016, **16**, 258.
102. B. Sun, O. Voznyy, H. Tan, P. Stadler, M. Liu, G. Walters, A. H. Proppe, M. Liu, J. Fan, T. Zhuang, J. Li, M. Wei, J. Xu, Y. Kim, S. Hoogland and E. H. Sargent, *Adv. Mater.*, 2017, **29**, 1700749.
103. Y. Kim, F. Che, J. W. Jo, J. Choi, F. P. García de Arquer, O. Voznyy, B. Sun, J. Kim, M.-J. Choi, R. Quintero-Bermudez, F. Fan, C. S. Tan, E. Bladt, G. Walters, A. H. Proppe, C. Zou, H. Yuan, S. Bals, J. Hofkens, M. B. J. Roeffaers, S. Hoogland and E. H. Sargent, *Adv. Mater.*, 2019, **31**, 1805580.
104. H. Tavakoli Dastjerdi, D. Prochowicz, P. Yadav and M. M. Tavakoli, *Nanoscale*, 2019, **11**, 22832-22840.
105. H. Tavakoli Dastjerdi, R. Tavakoli, P. Yadav, D. Prochowicz, M. Saliba and M. M. Tavakoli, *ACS Appl. Mater. Interfaces*, 2019, **11**, 26047-26052.
106. B.-R. Hyun, J. J. Choi, K. L. Seyler, T. Hanrath and F. W. Wise, *ACS Nano*, 2013, **7**, 10938-10947.
107. B. F. Spencer, M. A. Leontiadou, P. C. J. Clark, A. I. Williamson, M. G. Silly, F. Sirotti, S. M. Fairclough, S. C. E. Tsang, D. C. J. Neo, H. E. Assender, A. A. R. Watt and W. R. Flavell, *Appl. Phys. Lett.*, 2016, **108**, 091603.
108. M. Yuan, O. Voznyy, D. Zhitomirsky, P. Kanjanaboos and E. H. Sargent, *Adv. Mater.*, 2015, **27**, 917-921.
109. R. L. Z. Hoye, B. Ehrler, M. L. Böhm, D. Muñoz-Rojas, R. M. Altamimi, A. Y. Alyamani, Y. Vaynzof, A. Sadhanala, G. Ercolano, N. C. Greenham, R. H. Friend, J. L. MacManus-Driscoll and K. P. Musselman, *Adv. Energy Mater.*, 2014, **4**, 1301544.
110. X. Zhang and E. M. J. Johansson, *J. Mater. Chem. A*, 2017, **5**, 303-310.
111. M. Liu, F. P. G. de Arquer, Y. Li, X. Lan, G.-H. Kim, O. Voznyy, L. K. Jagadamma, A. S. Abbas, S. Hoogland, Z. Lu, J. Y. Kim, A. Amassian and E. H. Sargent, *Adv. Mater.*, 2016, **28**, 4142-4148.
112. F. Yang, Y. Xu, M. Gu, S. Zhou, Y. Wang, K. Lu, Z. Liu, X. Ling, Z. Zhu, J. Chen, Z. Wu, Y. Zhang, Y. Xue, F. Li, J. Yuan and W. Ma, *J. Mater. Chem. A*, 2018, **6**, 17688-17697.
113. Y. Cho, P. Giraud, B. Hou, Y.-W. Lee, J. Hong, S. Lee, S. Pak, J. Lee, J. E. Jang, S. M. Morris, J. I. Sohn, S. Cha and J. M. Kim, *Adv. Energy Mater.*, 2018, **8**, 1700809.
114. M. M. Tavakoli, A. Simchi, Z. Fan and H. Aashuri, *Chem. Commun.*, 2016, **52**, 323-326.
115. C. Cheng, M. M. Lee, N. K. Noel, G. M. Hughes, J. M. Ball, H. E. Assender, H. J. Snaith and A. A. R. Watt, *ACS Appl. Mater. Interfaces*, 2014, **6**, 14247-14252.
116. H. Tavakoli Dastjerdi, D. Prochowic, P. Yadav and M. M. Tavakoli, *Sustain. Energy Fuels*, 2019, **3**, 3128-3134.
117. D.-K. Ko, P. R. Brown, M. G. Bawendi and V. Bulović, *Adv. Mater.*, 2014, **26**, 4845-4850.

118. H. Aqoma, M. A. Mubarok, W. Lee, W. T. Hadmojo, C. Park, T. K. Ahn, D. Y. Ryu and S.-Y. Jang, *Adv. Energy Mater.*, 2018, **8**, 1800572.
119. X. Zhang and E. M. J. Johansson, *Nano Energy*, 2016, **28**, 71-77.
120. R. A. Street and A. Salleo, *Appl. Phys. Lett.*, 2002, **81**, 2887-2889.
121. M. Stewart, R. S. Howell, L. Pires and M. K. Hatalis, *IEEE Trans. Electron Devices*, 2001, **48**, 845-851.
122. P. R. Brown, R. R. Lunt, N. Zhao, T. P. Osedach, D. D. Wanger, L.-Y. Chang, M. G. Bawendi and V. Bulović, *Nano Lett.*, 2011, **11**, 2955-2961.
123. S. M. Mahpeykar, Q. Xiong and X. Wang, *Opt. Express*, 2014, **22**, A1576-A1588.
124. X. Zhang, C. Hägglund, M. B. Johansson, K. Sveinbjörnsson and E. M. J. Johansson, *Adv. Funct. Mater.*, 2016, **26**, 1921-1929.
125. M. M. Tavakoli, M. Nasilowski, J. Zhao, M. G. Bawendi and J. Kong, *Small Methods*, 2019, **3**, 1900449.
126. W. Shockley and H. J. Queisser, *J. Appl. Phys.*, 1961, **32**, 510-519.
127. R. D. Schaller and V. I. Klimov, *Phys. Rev. Lett.*, 2004, **92**, 186601.
128. R. J. Ellingson, M. C. Beard, J. C. Johnson, P. Yu, O. I. Micic, A. J. Nozik, A. Shabaev and A. L. Efros, *Nano Lett.*, 2005, **5**, 865-871.
129. J. Tauc, *J. Phys. Chem. Solids*, 1959, **8**, 219-223.
130. S. Kolodinski, J. H. Werner, T. Wittchen and H. J. Queisser, *Appl. Phys. Lett.*, 1993, **63**, 2405-2407.
131. M. C. Beard, K. P. Knutsen, P. Yu, J. M. Luther, Q. Song, W. K. Metzger, R. J. Ellingson and A. J. Nozik, *Nano Lett.*, 2007, **7**, 2506-2512.
132. J. E. Murphy, M. C. Beard, A. G. Norman, S. P. Ahrenkiel, J. C. Johnson, P. Yu, O. I. Mićić, R. J. Ellingson and A. J. Nozik, *J. Am. Chem. Soc.*, 2006, **128**, 3241-3247.
133. R. D. Schaller, M. Sykora, S. Jeong and V. I. Klimov, *J. Phys. Chem. B*, 2006, **110**, 25332-25338.
134. A. Pandey and P. Guyot-Sionnest, *Science*, 2008, **322**, 929-932.
135. C. Delerue, G. Allan, J. J. H. Pijpers and M. Bonn, *Phys. Rev. B*, 2010, **81**, 125306.
136. A. J. Nozik, M. C. Beard, J. M. Luther, M. Law, R. J. Ellingson and J. C. Johnson, *Chem. Rev.*, 2010, **110**, 6873-6890.
137. V. I. Klimov, *Appl. Phys. Lett.*, 2006, **89**, 123118.
138. G. Nootz, L. A. Padilha, L. Levina, V. Sukhovatkin, S. Webster, L. Brzozowski, E. H. Sargent, D. J. Hagan and E. W. Van Stryland, *Phys. Rev. B*, 2011, **83**, 155302.
139. V. Sukhovatkin, S. Hinds, L. Brzozowski and E. H. Sargent, *Science*, 2009, **324**, 1542-1544.
140. N. J. L. K. Davis, M. L. Böhm, M. Tabachnyk, F. Wisnivesky-Rocca-Rivarola, T. C. Jellicoe, C. Ducati, B. Ehrler and N. C. Greenham, *Nat. Commun.*, 2015, **6**, 8259.
141. C. M. Cirloganu, L. A. Padilha, Q. Lin, N. S. Makarov, K. A. Velizhanin, H. Luo, I. Robel, J. M. Pietryga and V. I. Klimov, *Nat. Commun.*, 2014, **5**, 4148.
142. D. A. Quansah and M. S. Adaramola, *Renew. Energy*, 2019, **131**, 900-910.

143. S. Kim, A. R. Marshall, D. M. Kroupa, E. M. Miller, J. M. Luther, S. Jeong and M. C. Beard, *ACS Nano*, 2015, **9**, 8157-8164.
144. J. Chang, Y. Kuga, I. Mora-Seró, T. Toyoda, Y. Ogomi, S. Hayase, J. Bisquert and Q. Shen, *Nanoscale*, 2015, **7**, 5446-5456.
145. Y. Zhang, C. Ding, G. Wu, N. Nakazawa, J. Chang, Y. Ogomi, T. Toyoda, S. Hayase, K. Katayama and Q. Shen, *J. Phys. Chem. C*, 2016, **120**, 28509-28518.
146. X. Zhang, C. Hägglund and E. M. J. Johansson, *Energy Environ. Sci.*, 2017, **10**, 216-224.
147. X. Zhang, D. Jia, C. Hägglund, V. A. Öberg, J. Du, J. Liu and E. M. J. Johansson, *Nano Energy*, 2018, **53**, 373-382.
148. X. Zhang, J. Zhang, D. Phuyal, J. Du, L. Tian, V. A. Öberg, M. B. Johansson, U. B. Cappel, O. Karis, J. Liu, H. Rensmo, G. Boschloo and E. M. J. Johansson, *Adv. Energy Mater.*, 2018, **8**, 1702049.
149. W. Ahmad, J. He, Z. Liu, K. Xu, Z. Chen, X. Yang, D. Li, Y. Xia, J. Zhang and C. Chen, *Adv. Mater.*, **0**, 1900593.
150. J. Tang, L. Brzozowski, D. A. R. Barkhouse, X. Wang, R. Debnath, R. Wolowiec, E. Palmiano, L. Levina, A. G. Pattantyus-Abraham, D. Jamakosmanovic and E. H. Sargent, *ACS Nano*, 2010, **4**, 869-878.
151. S. Kim, S. H. Im, M. Kang, J. H. Heo, S. I. Seok, S.-W. Kim, I. Mora-Seró and J. Bisquert, *Phys. Chem. Chem. Phys.*, 2012, **14**, 14999-15002.
152. M. Sykora, A. Y. Koposov, J. A. McGuire, R. K. Schulze, O. Tretiak, J. M. Pietryga and V. I. Klimov, *ACS Nano*, 2010, **4**, 2021-2034.
153. J. W. Jo, J. Choi, F. P. García de Arquer, A. Seifitokaldani, B. Sun, Y. Kim, H. Ahn, J. Fan, R. Quintero-Bermudez, J. Kim, M.-J. Choi, S.-W. Baek, A. H. Proppe, G. Walters, D.-H. Nam, S. Kelley, S. Hoogland, O. Voznyy and E. H. Sargent, *Nano Lett.*, 2018, **18**, 4417-4423.
154. A. Rivaton, S. Chambon, M. Manceau, J.-L. Gardette, N. Lemaître and S. Guillerez, *Polym. Degrad. Stab.*, 2010, **95**, 278-284.
155. J. Razzell-Hollis, J. Wade, W. C. Tsoi, Y. Soon, J. Durrant and J.-S. Kim, *J. Mater. Chem. A*, 2014, **2**, 20189-20195.
156. F. A. Soria, E. M. Patrito and P. Paredes-Olivera, *J. Phys. Chem. C*, 2012, **116**, 24607-24615.
157. J. Kim, H. Jung, J. Song, K. Kim and C. Lee, *ACS Appl. Mater. Interfaces*, 2017, **9**, 24052-24060.
158. O. Pachoumi, C. Li, Y. Vaynzof, K. K. Banger and H. Sirringhaus, *Adv. Energy Mater.*, 2013, **3**, 1428-1436.
159. Q. An, P. Fassl, Y. J. Hofstetter, D. Becker-Koch, A. Bausch, P. E. Hopkinson and Y. Vaynzof, *Nano Energy*, 2017, **39**, 400-408.
160. S. Chen, Y. j. Wang, Q. Liu, G. Shi, Z. Liu, K. Lu, L. Han, X. Ling, H. Zhang, S. Cheng and W. Ma, *Adv. Energy Mater.*, 2018, **8**, 1701194.
161. W. Nie, J.-C. Blancon, A. J. Neukirch, K. Appavoo, H. Tsai, M. Chhowalla, M. A. Alam, M. Y. Sfeir, C. Katan, J. Even, S. Tretiak, J. J. Crochet, G. Gupta and A. D. Mohite, *Nat. Commun.*,

2016, **7**, 11574.
162. D. H. Webber and R. L. Brutchey, *J. Am. Chem. Soc.*, 2012, **134**, 1085-1092.
163. H. Zhao, H. Liang, B. A. Gonfa, M. Chaker, T. Ozaki, P. Tijssen, F. Vidal and D. Ma, *Nanoscale*, 2014, **6**, 215-225.
164. H. Zhao, M. Chaker, N. Wu and D. Ma, *J. Mater. Chem.*, 2011, **21**, 8898-8904.
165. A. Bansal and N. S. Lewis, *J. Phys. Chem. B*, 1998, **102**, 4058-4060.
166. J. M. Salazar-Rios, N. Sukharevska, M. J. Speirs, S. Jung, D. Dirin, R. M. Dragoman, S. Allard, M. V. Kovalenko, U. Scherf and M. A. Loi, *Adv. Mater. Interfaces*, 2018, **5**, 1801155.
167. Y. I. Lee, N. J. Jeon, B. J. Kim, H. Shim, T.-Y. Yang, S. I. Seok, J. Seo and S. G. Im, *Adv. Energy Mater.*, 2018, **8**, 1701928.
168. W. J. Baumgardner, K. Whitham and T. Hanrath, *Nano Lett.*, 2013, **13**, 3225-3231.
169. F. Giberti, M. Vörös and G. Galli, *Nano Lett.*, 2017, **17**, 2547-2553.
170. A. Fischer, L. Rollny, J. Pan, G. H. Carey, S. M. Thon, S. Hoogland, O. Voznyy, D. Zhitomirsky, J. Y. Kim, O. M. Bakr and E. H. Sargent, *Adv. Mater.*, 2013, **25**, 5742-5749.
171. I. J. Kramer, G. Moreno-Bautista, J. C. Minor, D. Kopilovic and E. H. Sargent, *Appl. Phys. Lett.*, 2014, **105**, 163902.
172. R. Quintero-Torres, C. A. Foell, J. Pichaandi, F. C. J. M. v. Veggel and J. F. Young, *Appl. Phys. Lett.*, 2012, **101**, 121904.
173. N. J. Jeon, J. H. Noh, Y. C. Kim, W. S. Yang, S. Ryu and S. I. Seok, *Nat. Mater.*, 2014, **13**, 897.
174. M. Eslamian and F. Zabihi, *Nanoscale Research Letters*, 2015, **10**, 462.
175. J. M. Luther, M. Law, Q. Song, C. L. Perkins, M. C. Beard and A. J. Nozik, *ACS Nano*, 2008, **2**, 271-280.
176. W. K. Bae, J. Joo, L. A. Padilha, J. Won, D. C. Lee, Q. Lin, W.-k. Koh, H. Luo, V. I. Klimov and J. M. Pietryga, *J. Am. Chem. Soc.*, 2012, **134**, 20160-20168.
177. Y. Liu, J. Tolentino, M. Gibbs, R. Ihly, C. L. Perkins, Y. Liu, N. Crawford, J. C. Hemminger and M. Law, *Nano Lett.*, 2013, **13**, 1578-1587.
178. J. L. Ellis, D. D. Hickstein, K. J. Schnitzenbaumer, M. B. Wilker, B. B. Palm, J. L. Jimenez, G. Dukovic, H. C. Kapteyn, M. M. Murnane and W. Xiong, *J. Am. Chem. Soc.*, 2015, **137**, 3759-3762.
179. T. Cassagneau, T. E. Mallouk and J. H. Fendler, *J. Am. Chem. Soc.*, 1998, **120**, 7848-7859.
180. N. J. Thompson, M. W. B. Wilson, D. N. Congreve, P. R. Brown, J. M. Scherer, Thomas S. Bischof, M. Wu, N. Geva, M. Welborn, T. V. Voorhis, V. Bulović, M. G. Bawendi and Marc A. Baldo, *Nat. Mater.*, 2014, **13**, 1039.
181. Z. Jin, A. Wang, Q. Zhou, Y. Wang and J. Wang, *Sci. Rep.*, 2016, **6**, 37106.
182. H. Choi, J.-G. Lee, X. D. Mai, M. C. Beard, S. S. Yoon and S. Jeong, *Sci. Rep.*, 2017, **7**, 622.
183. C. Jiang, Z. Zhong, B. Liu, Z. He, J. Zou, L. Wang, J. Wang, J. Peng and Y. Cao, *ACS Appl. Mater. Interfaces*, 2016, **8**, 26162-26168.
184. T. M. Eggenhuisen, Y. Galagan, A. F. K. V. Biezemans, T. M. W. L. Slaats, W. P. Voorthuijzen, S. Kommeren, S. Shanmugam, J. P. Teunissen, A. Hadipour, W. J. H. Verhees, S. C. Veenstra,

M. J. J. Coenen, J. Gilot, R. Andriessen and W. A. Groen, *J. Mater. Chem. A*, 2015, **3**, 7255-7262.

185. S. G. Hashmi, D. Martineau, X. Li, M. Ozkan, A. Tiihonen, M. I. Dar, T. Sarikka, S. M. Zakeeruddin, J. Paltakari, P. D. Lund and M. Grätzel, *Adv. Mater. Technol.*, 2017, **2**, 1600183.
186. X. Lin, R. Klenk, L. Wang, T. Köhler, J. Albert, S. Fiechter, A. Ennaoui and M. C. Lux-Steiner, *Energy Environ. Sci.*, 2016, **9**, 2037-2043.
187. W. Ji, S. Liu, H. Zhang, R. Wang, W. Xie and H. Zhang, *ACS Photonics*, 2017, **4**, 1271-1278.
188. K.-J. Chen, H.-C. Chen, K.-A. Tsai, C.-C. Lin, H.-H. Tsai, S.-H. Chien, B.-S. Cheng, Y.-J. Hsu, M.-H. Shih, C.-H. Tsai, H.-H. Shih and H.-C. Kuo, *Adv. Funct. Mater.*, 2012, **22**, 5138-5143.
189. H. Li, K. Wu, J. Lim, H.-J. Song and V. I. Klimov, *Nat. Energy*, 2016, **1**, 16157.
190. L. Wengeler, B. Schmidt-Hansberg, K. Peters, P. Scharfer and W. Schabel, *Chem. Eng. Process.*, 2011, **50**, 478-482.
191. M. O. Reese, S. Glynn, M. D. Kempe, D. L. McGott, M. S. Dabney, T. M. Barnes, S. Booth, D. Feldman and N. M. Haegel, *Nat. Energy*, 2018, **3**, 1002-1012.
192. J. Jean, J. Xiao, R. Nick, N. Moody, M. Nasilowski, M. Bawendi and V. Bulović, *Energy Environ. Sci.*, 2018, **11**, 2295-2305.
193. A. Karani, L. Yang, S. Bai, M. H. Futscher, H. J. Snaith, B. Ehrler, N. C. Greenham and D. Di, *ACS Energy Lett.*, 2018, **3**, 869-874.
194. *http://www.iea-pvps.org/fileadmin/dam/public/report/statistics/2018_iea-pvps_report_2018.pdf*.
195. Z. Huang, G. Zhai, Z. Zhang, C. Zhang, Y. Xia, L. Lian, X. Fu, D. Zhang and J. Zhang, *CrystEngComm*, 2017, **19**, 946-951.
196. *http://pvinsights.com/ (accessed on Dec. 10, 2019)*.
197. M. M. Lunardi, D. R. Needell, H. Bauser, M. Phelan, H. A. Atwater and R. Corkish, *Energy*, 2019, **181**, 1-10.
198. M. R. Bergren, N. S. Makarov, K. Ramasamy, A. Jackson, R. Guglielmetti and H. McDaniel, *ACS Energy Lett.*, 2018, **3**, 520-525.
199. H.-J. Song, B. G. Jeong, J. Lim, D. C. Lee, W. K. Bae and V. I. Klimov, *Nano Lett.*, 2018, **18**, 395-404.
200. C. A. Nelson, N. R. Monahan and X. Y. Zhu, *Energy Environ. Sci.*, 2013, **6**, 3508-3519.
201. X. Huang, S. Han, W. Huang and X. Liu, *Chem. Soc. Rev.*, 2013, **42**, 173-201.
202. B. S. Richards, *Sol. Energy Mater. Sol. Cells*, 2006, **90**, 2329-2337.
203. Y. Bi, S. Pradhan, S. Gupta, M. Z. Akgul, A. Stavrinadis and G. Konstantatos, *Adv. Mater.*, 2018, **30**, 1704928.
204. *https://www.qdsolarinc.com/*.
205. O. Ouellette, N. Hossain, B. R. Sutherland, A. Kiani, F. P. García de Arquer, H. Tan, M. Chaker, S. Hoogland and E. H. Sargent, *ACS Energy Lett.*, 2016, **1**, 852-857.
206. R. W. Crisp, N. Kirkwood, G. Grimaldi, S. Kinge, L. D. A. Siebbeles and A. J. Houtepen, *ACS Appl. Energy Mater.*, 2018, **1**, 6569-6576.

207. M. Bernechea, N. C. Miller, G. Xercavins, D. So, A. Stavrinadis and G. Konstantatos, *Nat. Photonics*, 2016, **10**, 521.
208. D. So, S. Pradhan and G. Konstantatos, *Nanoscale*, 2016, **8**, 16776-16785.
209. *European Parliament, Council of the European Union, OJ 174 (European Parliament, Council of the European Union)*.
210. H.-J. Song, H. s. Yoon, Y. Ju, S. M. Kim, W. G. Shin, J. Lim, S. Ko, H. m. Hwang and G. H. Kang, *Solar Energy*, 2019, **184**, 273-280.
211. D. Hahm, J. H. Chang, B. G. Jeong, P. Park, J. Kim, S. Lee, J. Choi, W. D. Kim, S. Rhee, J. Lim, D. C. Lee, C. Lee, K. Char and W. K. Bae, *Chem. Mater.*, 2019, **31**, 3476-3484.
212. J.-H. Kim and H. Yang, *Chem. Mater.*, 2016, **28**, 6329-6335.
213. J. Lim, M. Park, W. K. Bae, D. Lee, S. Lee, C. Lee and K. Char, *ACS Nano*, 2013, **7**, 9019-9026.
214. S. Adachi, *J. Appl. Phys.*, 1989, **66**, 6030-6040.
215. S. Tamang, S. Lee, H. Choi and S. Jeong, *Chem. Mater.*, 2016, **28**, 8119-8122.
216. W. Liu, J.-S. Lee and D. V. Talapin, *J. Am. Chem. Soc.*, 2013, **135**, 1349-1357.
217. R. D. Schaller, J. M. Pietryga and V. I. Klimov, *Nano Lett.*, 2007, **7**, 3469-3476.
218. Y.-H. Won, O. Cho, T. Kim, D.-Y. Chung, T. Kim, H. Chung, H. Jang, J. Lee, D. Kim and E. Jang, *Nature*, 2019, **575**, 634-638.
219. J. R. Heath, *Chem. Soc. Rev.*, 1998, **27**, 65-71.
220. D. Franke, D. K. Harris, O. Chen, O. T. Bruns, J. A. Carr, M. W. B. Wilson and M. G. Bawendi, *Nat. Commun.*, 2016, **7**, 12749.
221. J. H. Song, H. Choi, H. T. Pham and S. Jeong, *Nat. Commun.*, 2018, **9**, 4267.
222. S. Lin, Y. Feng, X. Wen, P. Zhang, S. Woo, S. Shrestha, G. Conibeer and S. Huang, *J. Phys. Chem. C*, 2015, **119**, 867-872.
223. T. Englman, E. Terkieltaub and L. Etgar, *J. Phys. Chem. C*, 2015, **119**, 12904-12909.
224. K. Li, S. Wang, C. Chen, R. Kondrotas, M. Hu, S. Lu, C. Wang, W. Chen and J. Tang, *J. Mater. Chem. A*, 2019, **7**, 9665-9672.
225. Z. Li, X. Liang, G. Li, H. Liu, H. Zhang, J. Guo, J. Chen, K. Shen, X. San, W. Yu, R. E. I. Schropp and Y. Mai, *Nat. Commun.*, 2019, **10**, 125.
226. I. Repins, M. A. Contreras, B. Egaas, C. DeHart, J. Scharf, C. L. Perkins, B. To and R. Noufi, *Prog. Photovoltaics*, 2008, **16**, 235-239.
227. J. Du, Z. Du, J.-S. Hu, Z. Pan, Q. Shen, J. Sun, D. Long, H. Dong, L. Sun, X. Zhong and L.-J. Wan, *J. Am. Chem. Soc.*, 2016, **138**, 4201-4209.
228. H. J. Yun, J. Lim, A. S. Fuhr, N. S. Makarov, S. Keene, M. Law, J. M. Pietryga and V. I. Klimov, *ACS Nano*, 2018, **12**, 12587-12596.
229. A. S. Fuhr, H. J. Yun, N. S. Makarov, H. Li, H. McDaniel and V. I. Klimov, *ACS Photonics*, 2017, **4**, 2425-2435.